

A Comprehensive MARTINI Coarse-Grained Framework for Phyllosilicate Clay/Polymer Nanocomposites: From Atomistic Validation to Mesoscale Insights

Ankit Patidar* and Gaurav Goel*

*Department of Chemical Engineering, Indian Institute of Technology Delhi, City - New
Delhi, Postal code - 110016, India*

E-mail: Ankit.Patidar@chemical.iitd.ac.in; goelg@chemical.iitd.ac.in

Phone: 91 11 2659 1025

Abstract

Phyllosilicate clays have diverse applications in packaging industries and are found highly suitable for formulation, including thermoplastic starch (TPS), polyethylene (PE), or their combination. We developed CG MARTINI-3 parameters of the pyrophyllite using Lifshitz theory and experimental surface tension data. These initial bead assignments of pyrophyllite and periodic tetramethylammonium-montmorillonite (TMA-MMT) sheet were fine-tuned using optimal reproduction of structural, thermodynamic, and dynamic properties obtained via all-atom (AA) simulation of TPS with a periodic pyrophyllite sheet. These developed models predicted the correct AA radial distribution function and two-body excess entropy for polymer-sorbitol pairs, showcasing the robustness of the developed CG model in predicting the properties not used in parameterization. These composite simulation revealed acceleration (for pyrophyllite)

or retardation (for TMA–MMT) of khun segment dynamics (compared to melt) with the depletion of polymer near the surface. The developed CG parameters were used to investigate long-time ($\sim 10^3$ ns) behavior of large ($\sim 10^2$ nm) TPS-polyethylene (PE) melt and their Cloisite-15A-based composite systems. The coordination number indicated compatibilization of the TPS-PE phase, achieved by binding TPS through its bare polar surface and PE via alkyl-mediated interactions, which consequently reduced the TPS-PE interfacial surface tension from 45 mN m^{-1} to 13.06 mN m^{-1} . Additionally, high TPS-clay coordination, sustained localization of clay at the TPS-PE interface, and clay aggregation observed in CG simulation closely agree with experimental observations. Further, the CG model effectively captured the clay-mediated variation in overall morphology of the TPS-PE system and their direct impact on chain conformational properties, making this CG model highly suitable for a material design perspective.

1 Introduction

The environmental impact of synthetic materials like polyethylene (PE) in packaging waste has driven significant research into biopolymers.¹ Thermoplastic starch (TPS) could be used as an alternative due to its biodegradability,² Low cost, wide availability, and excellent film-forming properties (good transparency and low processing temperature).^{3,4} TPS formulation consisting of linear amylose (1-4 linked α -D glucose), amylopectin (amylose with additional 1-6 linked branches), and plasticizers (sorbitol, water, etc.),⁵ proven suitable option for food packaging and paper additive materials.^{6–10} However, its poor mechanical properties (low Young’s modulus and tensile strength, limited elongation at break)^{11–13} and low moisture resistance¹⁴ necessitate the addition of components with complementary properties, such as addition of nanofillers,^{15–17} blending with other polymers like PE.^{18,19} The optimal formulation, consisting of PE and TPS, has demonstrated good film-forming properties with the additional advantage of biodegradability.^{3,4} However, different polarities of TPS and PE lead to phase separation,^{20,21} which yields a material with poor mechanical proper-

ties.¹⁸ The compatibilization of polymer blends can be achieved by using nanoparticles,²¹ block copolymers,²² and Nano clay.^{15,23} The high surface-to-volume ratio, low cost, and easily achievable surface tuning in phyllosilicate clays have made it an attractive option for compatibilization purposes in packaging applications.¹⁵⁻¹⁷ Apart from the compatibilization, polymer nanocomposite also shows better mechanical, thermal, biodegradation, and barrier properties.^{11,15,23-26} For example, the addition of 5% Cloisite-15A clay (a surface-modified clay) in the TPS-PE with PE-grafted maleic anhydride blend decreased the diameter TPS domains from 500 nm to 200 nm) and this uniformity in morphology has improved the tensile strength by 35%.^{27,28} However, selecting the appropriate phyllosilicate for a specific formulation could be a time-consuming and cost-consuming exercise, and require optimization over a large parameter space, such as chemical composition, formulation of the base component, chemical structure of interacting polymer, the type of surface, etc. The compatibilization over multi-component systems with high chemical heterogeneity (branching in amylopectin and the presence of small molecules like sorbitol or water) further increases challenges in material design.

The MD simulations provide the structure-property relationship of multicomponent systems, which complement the material design by providing screening over a large parameter space.²⁹⁻³² MD simulation at all-atom (AA) scale has shown their application in accurate prediction of Young's modulus and glass transition temperature of TPS,^{33,34} the radius of gyration and density of PE,³⁵ and mechanical properties of tetramethylammonium-montmorillonite (TMA-MMT) clay.³⁶ However, the small time-step (1 fs) of the AA simulation, the polymer's large molecule weight with high relaxation time, and the large diameter of clay (~ 200 nm) make it computationally expensive or inaccessible in majority of the systems. For example, AA simulation of TPS-TMA-MMT consisting of smaller chains ($R_g \sim 2$ nm) and MMT sheet ($10.32 \text{ nm} \times 10.71 \text{ nm} \times 1.2 \text{ nm}$) took 10^9 steps to extract some meaningful properties of polymer near the surface.³³ Phenomena such as phase separation, occurring at time scales ranging from 10^1 s- 10^3 s, play a crucial role in material design but are currently

inaccessible through AA simulation.

The coarse-grain (CG) approaches represent groups of atoms as a single bead, significantly reducing the computational cost while capturing the essential properties relevant to the phenomenon under study. Some mesoscale methods like dissipative particle dynamics (DPD) simulations,³⁷⁻⁴⁵ field-based theories⁴⁶⁻⁵³ and integral-equation theories⁵⁴⁻⁵⁸ have been used extensively to study morphological, structural and thermodynamics properties of extensive large systems (10³nm). These methods used soft-core potential between larger chain units (\sim Kuhn length) and their values obtained from experiments or AA simulations. However, a small chemical modification at the monomer level can completely alter the material morphology,¹⁶ and these changes can not be directly captured in these methods. Also, the applicability of their parameters in certain temperature and pressure ranges, and increased difficulty in their estimation for complex formulation make them inefficient models for the present system.

Chemical-specific CG models model (bead size \sim nm) like iterative Boltzmann inversion (IBI),^{59,60} force matching⁶¹ and MARTINI CG force field⁶² combine only 4-10 atoms in one bead and therefore provide better chemical representation with at least 100 times speed up as compared to AA simulation. However, IBI and force matching methods do not provide chemical transferability and even temperature transferability obtained by optimizing the parameters using data from multiple state points.⁶³ The MARTINI-FF, based on partitioning energy between polar and apolar solvents, provided good transferability across diverse state-points,⁶² and proven application in estimating correct interfacial properties of solvents,⁶⁴ making it a suitable choice for the present system. The MARTINI-2 force field parameters for PE,³⁵ TPS,^{33,65} and phyllosilicate nanocomposites³⁶ are well-established. Their combined implementation in the PE-TMA-MMT system successfully reproduced all-atom chain properties and PE structural density profiles near TMA-MMT clay across temperatures, confirming strong parameter transferability across chemical environments and state points.³⁶ However, some rescaling in cross-interaction was required to avoid freezing near

the surface.^{33,66–68} The MARTINI-2 FF parameters of other TPS components like sorbitol⁶⁹ and polysaccharides^{70,71} also overestimate the solute-solvent interactions, making their results doubtful for highly complex polymer nanocomposite systems. The recently introduced MARTINI-3 FF parameters eliminated these limitations, making it an ideal forcefield to study highly heterogeneous systems in different operating conditions.⁷² Additionally, several carbohydrate models including linear 1–4 α -D glucose and branched 1–6 α -D glucose are available in the literature.^{73,74} However, to the best of our knowledge, the MARTINI-3 model of pyrophyllite or any surface-modified MMT is not available in the literature.

Given the wide interest in phyllosilicate-based composites, we have developed MARTINI-3 CG FF parameters for pyrophyllite and TMA-MMT clay using a combination of experimental and MD simulation data. The hydration energies obtained from experimental surface tension data were used for initial surface bead assignments of pyrophyllite, which were fine-tuned based on optimal reproduction of AA structural (radius of gyration), thermodynamic (two-body excess entropy, density, conformational entropy), and dynamic properties (diffusion coefficient) of TPS near pyrophyllite clay. The same set of AA properties in TPS–[tetramethylammonium (TMA)]-MMT composite was used to determine the optimal bead assignments for the TMA-MMT surface. Additionally, this study reported some key observations, including the dependency of polymer properties on the nature of the polymer-clay interaction.

Further, the developed CG model was used to investigate the effect of Cloisite-15A compatibilizers on the morphological and interfacial behavior of a large TPS-PE system. The physical insights obtained by these CG simulations provided a quantitative agreement with some experimental studies,^{28,75} proving the robustness of models in material design.

2 Methods

2.1 System Details

MARTINI Force Field (FF) parameters for pyrophyllite and TMA-MMT clays were developed through AA and CG simulations of TPS melt, TPS-pyrophyllite (TPS-PY), and TPS-TMA-MMT composites. These parameters were subsequently utilized to simulate larger systems, including TPS-PE melt and TPS-PE-CL composites. More details on these systems are provided in Table 1.

Table 1: System details For each system studied, this table lists the weight percentage (wt %) of its components and the total number of beads employed in both AA (n_{AA}) and CG (n_{CG}) simulations. All the simulation performed at 613 K and 1 bar.

System	components	wt %	n_{AA}	n_{CG}
TPS	amylopectin, amylose, sorbitol, water	50 %, 20 %, 29 %, 1 %	55327	9123
TPS-PY	TPS, periodic pyrophyllite clay	80 %, 20 %	120254	21126
TPS-TMA-MMT	TPS, periodic TMA-MMT clay	82.5 %, 17.5 %	122974	21286
TPS-PE	TPS without water, PE	50 %, 50 %	-	338688
TPS-PE-Cl	TPS without water, PE, Cloisite-15A clay	47.5 %, 47.5 %, 5 %	-	366848

2.1.1 AA System and Simulation Details

AA structures and force field parameters of amylose (linear chain with eighteen α -D glucose monomers), amylopectin (a primary chain comprising twenty-seven α -D glucose monomers and a secondary branch composed of nine monomers), and sorbitol were obtained from CHARMM-GUI.⁷⁶⁻⁷⁸ The INTERFACE force field was employed to model pyrophyllite and TMA-MMT,⁷⁹ alongside the TIP3P water model. Packmol⁸⁰ was used to obtain a low-density TPS system ($\rho = 117.62 \text{ kg m}^{-3}$), which underwent multiple box rescaling and temperature-pressure (T - P) annealing cycles to obtain a high-density ($1227.62 \text{ kg m}^{-3}$) equilibrated system (more details are provided in section 5.1). The TPS composite systems consist of pyrophyllite (TPS-PY) and TMA-MMT (TPS-TMA-MMT) sheets were obtained

by sandwiching respective periodic sheets ($10.32 \text{ nm} \times 10.71 \text{ nm} \times 1.2 \text{ nm}$ connected across x - y periodic boundaries) between two well equilibrated TPS melt boxes (an equilibrated morphology TPS-TMA-MMT system shown in Figure S2 (a)).

AA MD simulations were performed using GROMACS 2024.2,⁸¹ with a time step of 1 fs, V-rescale thermostat ($\tau=1 \text{ ps}$), and either the Berendsen barostat ($\tau=2 \text{ ps}$, first 100 ns) or the Parrinello-Rahman barostat ($\tau=5 \text{ ps}$).

2.1.2 CG System and Simulation Details

The MARTINI CG parameters for amylose and amylopectin were taken from the polysaccharide CG model based on AA simulations of mono- and disaccharides in polar and apolar solvents.⁷³ Accordingly, we used the following bead assignments: (tiny) TP3 bead for hydroxymethyl, (small) SN4 for the ring oxygen, anomeric carbon, and the reduced-end anomeric hydroxyl, P3 for diol, and SN4 for the hydroxyethyl groups (see Figure 1 for mapping scheme). The sorbitol was modeled using three P3-type beads, each representing a diol group (Figure 1 (c)). The center of geometry (COG) positions of these diol groups were used to estimate bond and angle parameters of sorbitol (see Figure S6 for distribution). The CG structure and parameters of PE were generated from Polyply software.⁷⁴ The CG bonded parameters for the clays were taken from Khan,³⁶ who showed a good agreement between AA and CG simulation results for Young’s modulus and bending stiffness for these clays. The octahedral AlOH_2 groups in both pyrophyllite and TMA-MMT clays were represented using SN4a-type CG beads due to their structural similarities with acetal groups. However, the isomorphic substitution of Al^{3+} with Mg^{2+} in the octahedral layer of TMA-MMT generates a net negative charge, which is compensated by $+1 e$ charged TMA counterions. These MgOH_2 and TMA ions were represented by the charged SQ5 and Q2 beads, respectively. Clay materials exhibit distinct cleavage patterns, forming edges such as 110, 010, 101, and 130. We modeled the clay edges using the most stable 010 and 100 configurations, which feature surface SiOH groups and inner Al sites with one or two hydroxyl groups, respectively.

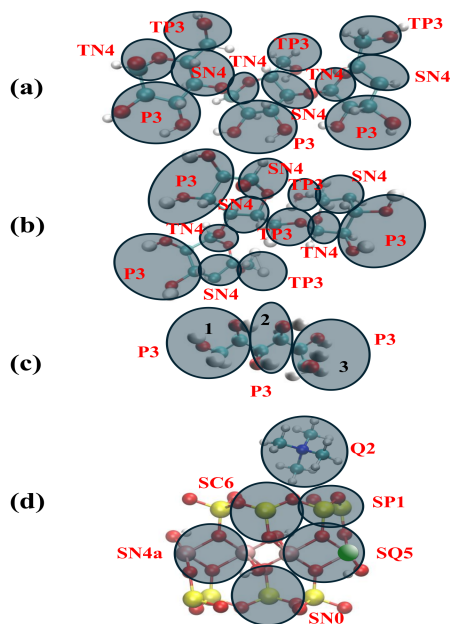


Figure 1: CG MARTINI mapping scheme for TPS and TMA-MMT clay. (a) trimeric segment of α -D-glucose units connected with 1–4 linkage (representing a small unit of linear amylose chain). (b) 1–4 linked trimeric segment of α -D-glucose with an additional 1–6 connectivity (represent branching in amylopectin). (c) sorbitol. (d) A TMA-MMT unit cell illustrating one octahedral *Al*-for-*Mg* substitution, resulting in $-1e$ charge balanced by $+1e$ TMA ion. Pyrophyllite clay contains no substitutions or counter ions. Red, white, cyan, yellow, pink, and green represent oxygen, hydrogen, carbon, silicon, aluminum, and magnesium atoms, respectively. Atoms within shaded circles are represented by a single CG bead, with the bead number (black) and type (red) labeled.

The *Al* sites on the 010 edge were assigned bead type P2 (hemiacetal-like), and those on the 100 edge were assigned P4 (hydroxyl-like), while surface SiOH groups on both edges were represented using P2 bead type. The MgOH_2 groups were consistently mapped to SQ5, regardless of their position (edge or inner). These assignments maintained an accurate representation of functional group chemistry according to the MARTINI-3 framework, while preserving relative polarity differences between edge types.⁷² For instance, 010 edge has relatively lower sorption energy ($-38.9 \text{ kJ mol}^{-1}$) compared to 100 edge ($-57.7 \text{ kJ mol}^{-1}$),⁸² and therefore represented by relatively lower-polarity bead combinations (P2 and P4). The CG bead-type for surface SiO_2 of pyrophyllite was selected based on hydration energies, which were calculated from experimental contact angle values of polar and apolar liquids on the pyrophyllite surface.⁸³ This MARTINI model of pyrophyllite was tested by comparing the structural arrangement and dynamic behavior of hexadecane, propanol, ethanol, isopropanol,

and sorbitol near the surface to AA simulation results. For relative comparison, CG simulations using some other surface bead assignments (SC4, SN2, SN4, SN6, and SP2) were also performed for each solvent-sheet system. Further, TPS-pyrophyllite (TPS-PY) nanocomposite simulations were performed to fine-tune these surface bead assignments using AA structural, thermodynamic, and dynamic properties. Similarly, we used AA properties from TPS-TMA-MMT composite simulations to obtain an optimal bead assignment of surface SiO_2 for TMA-MMT. We observed that the substitution of octahedral *Al* with *Mg* in TMA-MMT increased the surface polarity as compared to pyrophyllite, which necessitates the use of an additional surface bead-type to account for this local polarity. Therefore, one-third of surface SiO_2 coordinating with octahedral *Mg* through bridging oxygen are represented using high-polarity CG bead (see Figure 1). More details on bead assignment are provided in section 3.2.3.

The CG systems of TPS melt, TPS-PY, and TPS-TMA-MMT were directly prepared by placing CG beads at the center of mass positions (using Equation S6) of constituent atoms (mapping scheme in Figure 1) from well-equilibrated AA structures. A 50-50 wt% phase-separated TPS-PE melt CG system was prepared in Packmol using long polymer chains exceeding entanglement lengths: amylose (300-mer), amylopectin (1,300-mer), polyethylene (3,000-mer), and sorbitol (see Table 1 for details). This system contains a highly branched amylopectin structure where linear chains of sixteen and thirty-six α -D-glucose monomers are grafted to the main chain at ten- and twenty-monomer intervals, respectively. The TPS composition in this system mirrored the TPS melt system (see Table 1), except that the water fraction was replaced with sorbitol. A TPS-PE-Cl (5 phr) composite system was prepared by adding Cloisite-15A clay tactoids ($x \times y = 10.32 \text{ nm} \times 10.71 \text{ nm}$) to this TPS-PE system, with two tactoids positioned at the PE-TPS interface and two within the PE bulk to ensure clay dispersion across both phases. The Cloisite-15A clay was prepared by grafting C16 alkyl chains (represented by three C1 and one Q2 type CG bead) onto the MMT surface, with its equilibrated structure then used to form a two-clay tactoid assem-

bly (Figure S4). These systems represent only a small fraction of the TPS-PE interface formed between TPS droplets and the surrounding PE matrix, as observed in experimental studies.^{28,84} The TPS-PE melt and TPS-PE-CL composite systems obtained from Packmol underwent rescaling and temperature-pressure (T-P) annealing cycles to obtain well-packed systems of 24.11 nm × 24.59 nm × 53.12 nm and 24.82 nm × 24.58 nm × 57.15 nm, respectively (equilibrated TPS-PE-CL composite system is shown in Figure S3). The system annealed between 613K and 913K with steps of 50K, at each step system was energy minimized followed by 5 ns NPT simulation for local equilibration, more details about the annealing protocols discussed in section 5.1.

In all CG simulations, the system was coupled to the V-rescale thermostat ($\tau = 1$ ps) using a time step of 5 fs. The melt, TPS-TMA-MMT and TPS-PY-MMT composite system were coupled using Berendsen barostat ($\tau = 8$ ps, first 100 ns) or the Parrinello-Rahman barostat ($\tau = 40$ ps). However, for accurate estimation of interfacial properties, we used the semi-isotropic (NP_zT) pressure coupling using Berendsen barostat for TPS-PE melt and TPS-PE-CL composite systems. The CG potential is given as per Equation 1.

$$\begin{aligned}
 U = 4\epsilon_{ij} \left[\left(\frac{\sigma_{ij}}{r_{ij}} \right)^{12} - \left(\frac{\sigma_{ij}}{r_{ij}} \right)^6 \right] + \frac{q_i q_j}{4\pi\epsilon_0\epsilon_{rel}r_{ij}} \\
 + \frac{1}{2}K_l(l_{ij} - l_0)^2 + \frac{1}{2}K_\theta(\cos\theta_{ijk} - \cos\theta_0)^2 \\
 + K_\phi[1 + (\cos\phi_{ijkl} - \cos\phi_0)] \quad (1)
 \end{aligned}$$

where σ_{ij} , ϵ_{ij} , q , and ϵ_{rel} are bead diameter, interaction strength, bead charge, and relative dielectric constant, respectively. The force constant for bond (l_{ij}), angle (θ_{ijk}), and torsion (ϕ_{ijkl}) potentials are K_l , K_θ , and K_ϕ , respectively. The σ_{ij} values can change from 0.34 to 0.62 depending on the size of interacting beads, which could be regular, small, or tiny. The choice of ϵ_{ij} is linked to the functional group(s) in the CG bead, with primary categorization defined as polar (P), intermediate/nonpolar (N), apolar (C), halo-compounds (X), monovalent ions (Q), divalent ions (D) or water (W). Except for W and D beads, all beads

have subtypes characterized by an integer value ranging from 0 to 6, which indicates their interaction strength.

2.2 Property Calculation

In the TPS–TMA–MMT and TPS–PY–MMT composite systems, the near- and far-sheet regions were classified based on density profiles of polymer and sorbitol along the normal (z -axis) to the surface (marked by the dashed red vertical line in Figure 2). The center of mass (COM) distance of the polymer’s trimetric segment (\sim persistence length (0.86 nm) of amylose) from the sheet was used to classify it as a near or a far segment, with a chain labeled as a near/far-region chain if $> 70\%$ segments were in the near/far region. All properties of the melts and composites were evaluated at 613 K, while the solvent properties were analyzed at 300 K.

2.2.1 Structural and Dynamic Properties

We used in-built GROMACS utilities to calculate the density profiles (ρ_n), radius of gyration (R_g), and radial distribution function (RDF) of melt and composite systems. The density profile integrals Ar and Ln were calculated using Equation 2 and 3, respectively.

$$Ar = \int_0^z \rho(z) dz \quad (2)$$

$$Ln = \frac{1}{Ar} \int_0^z \rho(z) z dz \quad (3)$$

COG of atoms making the CG beads were used for RDF calculation in the AA simulations to allow comparison with the CG simulations. For the composite system, a 2D RDF was calculated in 0.37 nm slices parallel to the TMA–MMT sheet in the $x - y$ plane. The data is reported as average over four slices in the near region and five slices in the far region. The morphological evolution of TPS-PE melt and TPS-PE-Cl composite systems was evaluated using coordination number (CN) - time graphs. The CN of all possible pairs among TPS,

PE, and Cl was calculated using Equation 4,

$$\text{CN} = \rho_{\beta} \int_0^{r_{\text{cut}}} 2\pi r^2 g_{\alpha\beta}(r) dr \quad (4)$$

where, $g_{\alpha,\beta}(r)$ is RDF of these individual pairs, r_{cut} in cut-off distance, and ρ_{β} is number density of β component. The r_{cut} was chosen to be 1.1 nm, a value that corresponds to the second minima distance observed in RDF (Figure S13). The exclusions of up to five, three, and nine CG-bonded neighbors were used for the TPS, PE, and CL, respectively. We used small 10 ns trajectory (at 613 K) portion from each annealing cycle, full 25 ns *NVT* trajectory, and 50 ns blocks over full 1500 ns simulation for CN calculations. Diffusion coefficients of amylose and amylopectin trimetric segments were calculated from mean-square-displacement ($MSD(t)$) profiles using Einstein's Equation 5), with normalized diffusion coefficients (D_n) calculated as the lateral diffusion ratio (in the $x - y$ plane) relative to the melt ($D_n = D_{\text{composite}}/D_{\text{melt}}$).

$$\text{MSD}(t) = 6 \cdot D \cdot t \quad (5)$$

This normalization allowed the direct comparison of D_n values obtained from AA and CG simulations.

2.2.2 Thermodynamic Properties

The pairwise ($S_{2,\alpha\beta}$) and total (S_2) two-body excess entropies were calculated using the corresponding RDFs ($g_{\alpha,\beta}$) as per Equations 6 and 7 (integral calculated up to 2.5 nm), respectively,⁸⁵

$$S_{2,\alpha\beta} = -2\pi\rho \int_0^{\infty} g_{\alpha\beta}(r) \ln g_{\alpha\beta}(r) - [g_{\alpha\beta}(r) - 1] r^2 dr \quad (6)$$

$$S_2 = \sum_{\alpha,\beta} x_\alpha x_\beta S_{\alpha,\beta}, \quad (7)$$

, where, x_α and x_β are the mole fractions of the α and β components, respectively. The $S_{2,\alpha\beta}$ of composite systems were estimated using Equation S5. The configurational entropies (S_c) of amylose and amylopectin chains were calculated from the covariance matrix of each chain (after removing rigid-body translational and rotational motion) using Schlitter’s equation,⁸⁶ implemented with GROMACS utility anaeig.

2.2.3 Interfacial Tension Calculations

The Interfacial tensions of the TPS-PE melt and TPS-PE-CL composite were calculated using the method of Irving and Kirkwood (IK) (Equation 8),⁸⁷

$$\gamma = \int_{-L(z/2)}^{L(z/2)} (P_N(z) - P_T(z)) dz = \frac{1}{2} \langle P_N - P_T \rangle L_z \quad (8)$$

where $P_N(z) = P_{zz}(z)$ and $P_T(z) = \frac{1}{2}(P_{xx}(z) + P_{yy}(z))$ are normal and tangential pressure tensor components of the simulation box (length= L_z), respectively. The γ values were calculated in blocks of 100 ns over a trajectory length of 1500 ns, and errors were reported for converged trajectories.

3 Results and Discussion

3.1 Physical Insights from AA Simulation of Composites

We observed that the water and sorbitol density peaks near the surface became sharper when the surface was switched from a lower polarity PY surface to a higher polarity TMA-MMT surface (Figure 2), resulting in a more pronounced depletion of polymer near the surface. The increased polarity can be attributed to the presence of charged TMA ions, which facilitate the accumulation of polar TPS constituents such as sorbitol and water. This finding aligns with

experiments indicating that higher water content in the TPS–Cloisite (a bentonite nanoclay) composites promotes TPS intercalation and clay swelling.⁸⁸ Although the polymer seems depleted near the TMA–MMT surface, it shows a sharp increase ($\sim 50\%$ of the bulk value) in density within the first solvation layer. The presence of the hydroxyl group in amylose, amylopectin, and sorbitol might be the key reason for their mixing in the near-surface region. All component densities become identical to the bulk value at an average z -distance of 2.5 nm from the sheet, indicating minimal clay’s effect on the TPS beyond this distance. Therefore, this plane (shown by red line in Figure 2) was used to differentiate near and far clay regions for subsequent calculation of all reported properties. The polymer-surface interactions are directly linked to polymer dynamics. For example, the AA simulation of polyethylene oxide with Na–MMT (favorable interaction) indicated a slowdown in polymer dynamics,⁸⁹ and the opposite was observed upon the addition of repulsive nanoparticles to an LJ polymer.^{90,91} The D_n of amylose and amylopectin trimeric segments in the vicinity of pyrophyllite clay were 1.30 and 1.60, respectively (Table 2). However, these respective D_n were decreased to 0.96 and 1.16 in the near regions of TMA–MMT (Table 3), indicating increased favorable interactions within the TMA–MMT system. These results strongly align with experimental findings in which favorable TPS–MMT interactions promote effective exfoliation and enhance key material properties, including Young’s modulus, glass transition temperature, and moisture resistance.^{23,92,93} Additionally, a high water contact angle (100°) over the pyrophyllite surface indicated its nonpolar nature,⁸³ making it a repulsive surface for polar formulation like TPS (as observed in this study).

Further, the near-to-melt S_c ratios for amylose (1.03) and amylopectin (1.04) in the TPS–PY system suggested neutral or repulsive polymer-sheet interactions, which decreased to 0.99 and 0.92 respectively in the TPS–TMA–MMT system, demonstrating enhanced interfacial adhesion in the latter composite. However, the reduction in S_c from the melt state to the TPS–TMA–MMT system remains modest, suggesting weakly attractive polymer-sheet interactions. A similar decrease ($\sim 10\%$) in S_c was reported for polyethylene, polypropylene, and

polystyrene near TMA-MMT, a case of weakly attractive interaction.³⁶ We observed similar R_g for both polymers (amylose and amylopectin) in the near regions of the PY (1.34, 1.72) and TMA-MMT (1.32, 1.72), and both were slightly lower than melt values (1.38, 1.83). These findings contrast with previous reports, where attractive interactions in polyethylene oxide/Na-MMT systems led to a twofold increase in R_g ,⁸⁹ while repulsive surfaces resulted in negligible changes in the R_g of LJ polymers.⁹⁰ However, the strong solvent-surface affinity and interfacial polymer-plasticizer mixing (as evident in the density profiles) likely drive this deviation from conventional attractive/repulsive surface behavior.

The properties obtained from these AA simulations were used to complement the development of clay surface CG parameters obtained via Lifshitz theory over experimental contact angle data. The inclusion of multiple properties is expected to improve the model’s accuracy in capturing the free energy of surface adsorption. For example, adding miscibility trend data along with partition-free energies improved balance between solute-solvent interaction in recently released MARTINI-3 FF.^{62,72}

3.2 Development of CG Parameters

3.2.1 CG Parameters TPS Melt

The accuracy of the MARTINI CG parameters for amylose, amylopectin, and sorbitol was initially validated within a TPS melt system, using reference all-atom (AA) simulation results. The RDF obtained using AA and CG simulation had an excellent agreement in polymer-polymer and sorbitol-sorbitol pairs, resulting in less than 5% error in two-body excess entropies. However, a small outward shift in sorbitol-polymer RDF resulted in higher S_2 CG simulation (see Figure S11), which indicates small room for improvement in cross-interaction parameters. It was also observed that CG simulation gave more expanded structures of the polymer chains, which resulted in a significant higher R_g ($\approx 18\%$) and slightly lower S_c (6-8%) of amylose and amylopectin chains (see Table 2). These deviations in chain-

level properties can be removed by deriving the parameters over a longer polysaccharide chain, as done in our previous work.³³ Additionally, the model overestimated the TPS density (1280.7 kg m^{-3}) compared to AA simulations (1214.7 kg m^{-3}) at 613 K, but provided an improvement over MARTINI2 model (1141.1 kg m^{-3}).⁶⁵ Overall, the CG MARTINI-3 model demonstrates small improvements in chain- and system-level properties of the TPS melt while achieving marked enhancements in bead-level properties compared to the MARTINI2 model.

3.2.2 CG Non-bonded Parameters for Pyrophyllite Surface

We used Lifshitz theory over experimental contact angle data to derive hydration energies of the pyrophyllite surface (Equation S3), which was utilized to derive the MARTINI bead type for the surface. We obtained the hydration energy of 2.31 kJ mol^{-1} using experimental contact angle values of non-polar (α -bromonaphthalene and diiodomethane) and polar (water and ethylene glycol) liquids over pyrophyllite clay (more details are provided in section 5.3).⁸³ It was reported that MARTINI-3 FF overestimates the hydration energy, but the relative trend for different polarity liquids is maintained throughout. Therefore, the obtained hydration energy value was extrapolated using the best-fit line of experimental and simulation hydration energies of thirty-six solvents (see Equation S4).⁷² We found that the extrapolated hydration energy of $-1.65 \text{ kJ mol}^{-1}$ closely matches that of the SC6 bead ($-2.00 \text{ kJ mol}^{-1}$), confirming it as an appropriate choice for the pyrophyllite surface. Additionally, the selected bead-type imparts surface hydrophobicity, consistent with experimental studies reporting dispersive nature of surface⁸³ and low water-sorption energies (1 kJ mol^{-1}).⁸²

The density profiles along the z -direction of pyrophyllite sheet (Figure S5) and normalized diffusion coefficient (D_n , see Table S1) values obtained from CG simulations were nearly identical across different surface bead types for each solvent (hexadecane, propanol, ethanol, isopropanol, and sorbitol) studied, highlights entropic interaction dominance in these systems. Additionally, lower D_n values in CG simulations, relative to AA simulations, suggest

that the MARTINI-3 Force Field overestimates cross-interactions in these systems. We expect that this overestimation should increase with the molecular weight of the molecule as observed in glycans,⁷⁰ making polymer nanocomposite systems particularly suitable for rigorous evaluation and optimization of CG parameters. Therefore, AA MD simulations of the TPS-PY composite were employed to systematically refine the CG interaction parameters, ensuring fidelity to atomic-scale interfacial behavior. The CG simulations of the TPS-PY composite were conducted using surface beads of varying polarity (SC4, SC6, SN2, SN4, and SP2) to systematically compare structural, thermodynamic, and dynamic properties with those obtained from AA simulations (results shown in Table 2).

Table 2: Comparison of properties obtained from AA and CG of TPS melt and TPS-PY composite system The properties obtained from AA simulation compared against various CG models, each employing a different representation of the surface SiO_2 using SC6-SP2 type beads. The average values of radius of gyration (R_g), configuration entropy per CG bead (S_c), and normalized diffusion coefficient (D_n) were calculated using last 900 ns simulation trajectories obtained at 613 K and 1 bar.

		Amylose			Amylopectin			
		bead-type	near	far	melt	near	far	melt
$R_g(\text{nm})$	AA		1.34	1.35	1.38	1.72	1.80	1.83
	CG	C4	1.60	1.65	1.65	2.09	2.14	2.16
		SC6	1.59	1.64	1.65	2.07	2.15	2.16
		SN2	1.62	1.62	1.65	2.12	2.16	2.16
		SN4	1.57	1.64	1.65	2.07	2.14	2.16
		SN6	1.59	1.62	1.65	2.04	2.15	2.16
		SP2	1.57	1.63	1.65	2.05	2.16	2.16
$\langle S_c \rangle$ ($\text{J mol}^{-1} \text{K}$)	AA		39.24	40.22	37.97	40.86	43.12	39.30
	CG	SC4	33.77	36.34	34.91	37.10	38.29	36.87
		SC6	34.31	36.18	34.91	36.23	38.34	36.87
		SN2	33.32	35.72	34.91	36.50	39.00	36.87
		SN4	33.66	36.29	34.91	35.15	39.28	36.87
		SN6	33.11	36.46	34.91	34.66	37.82	36.87
		SP2	34.01	48.54	36.18	36.43	39.25	36.87
D_n	AA		1.30	-	-	1.60	-	-
	CG	SC4	0.65	-	-	0.84	-	-
		SC6	0.74	-	-	0.82	-	-
		SN2	0.70	-	-	0.65	-	-
		SN4	0.23	-	-	0.32	-	-
		SN6	freezing	-	-	freezing	-	-
		SP2	freezing	-	-	freezing	-	-

Table 3: Comparison of properties obtained using AA and CG simulations of TPS melt and TPS-MMT-TMA composite The properties obtained from atomistic (AA) simulations were compared against various coarse-grained (CG) models, where the surface SiO_2 are represented by two types of CG beads: two-thirds by SC6 (common to all CG models) and one-third beads by SN6-SP6 beads that differ in polarity across the models. The average values of radius of gyration (R_g), configuration entropy per CG bead (S_c), and normalized diffusion coefficient (D_n) were calculated using last 900 ns simulation trajectories obtained at 613 K and 1 bar.

		Amylose			Amylopectin			
		bead-type	near	far	melt	near	far	melt
$R_g(\text{nm})$	AA		1.32	1.36	1.38	1.72	1.77	1.83
	CG	SN6	1.59	1.64	1.65	2.07	2.15	2.16
		SP1	1.61	1.64	1.65	2.13	2.12	2.16
		SP2	1.55	1.64	1.65	2.11	2.15	2.16
		SP4	1.60	1.64	1.65	2.09	2.14	2.16
		SP6	1.59	1.61	1.65	2.08	2.12	2.16
$\langle S_c \rangle$ ($\text{J mol}^{-1} \text{K}$)	AA		37.72	39.11	37.97	36.23	41.92	39.30
	CG	SN6	34.42	36.40	34.91	36.01	40.01	36.87
		SP1	34.27	36.20	34.91	36.75	40.21	36.87
		SP2	34.12	36.29	34.91	36.02	39.35	36.87
		SP4	34.14	36.53	34.91	36.25	39.54	36.87
		SP6	34.83	36.54	34.91	36.10	40.10	36.87
D_n	AA		0.96	-	-	1.16	-	-
	CG	SN6	0.99	-	-	0.94	-	-
		SP1	0.74	-	-	1.00	-	-
		SP2	0.74	-	-	0.79	-	-
		SP4	0.67	-	-	0.79	-	-
		SP6	0.66	-	-	0.84	-	-

It was observed that any increase in the polarity level beyond SN2 resulted in the freezing of kuhn segments near the surface and high relative error in density profile integrals of polymer and sorbitol (Figure S7), making them unsuitable bead choices for the surface. Even the lower polarity beads SC4 and SC6 did not reproduce accurate AA D_n (relative error $\sim 50\%$), but effectively prevented freezing of polymer near the surface and provided a better agreement with AA density distributions of TPS constituents. The observation indicated that the MARTINI-3 force field parameters struggle to accurately capture interfacial interactions, a challenge that has also been noted in other systems. For instance, standard MARTINI-3 parameters fail to accurately describe protein-membrane interfaces due to in-

sufficient hydrophobic interactions, necessitating both reduced protein–water interactions and enhanced protein–lipid hydrophobic interactions for improved interfacial structure and membrane curvature prediction.⁹⁴ The SC4 and SC6 bead types most accurately replicated

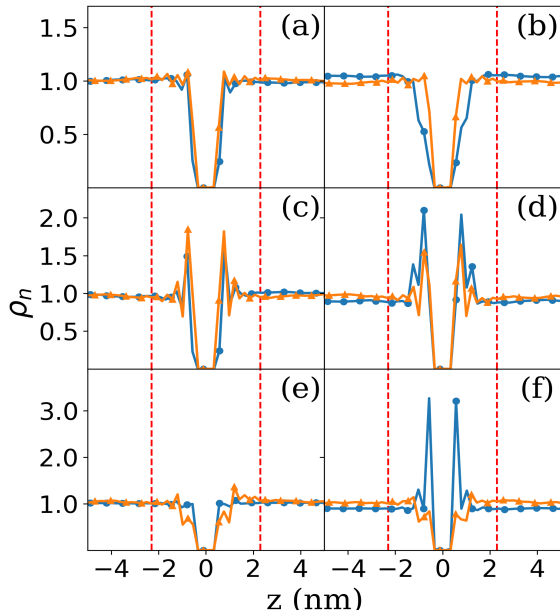


Figure 2: Normalized density profile of TPS-PY and TPS-MMT composite. The density profiles of polymer, sorbitol, and water in normal z direction of the pyrophyllite (a, c, e) and TMA-MMT (b, d, f) sheets were obtained using AA (—●—) and CG (—▲—) simulations of TPS composite systems. The obtained density profiles were normalized relative to the TPS melt density, with all simulations performed at $T = 613\text{ K}$ and $P = 1\text{ bar}$.

density profiles of sorbitol and polymer, showing relative errors of 13.17% and 4.31% in polymer A_r , and 10.21% and 11.95% in sorbitol A_r , respectively (see Figure S7 for all the data). The average (over sorbitol and polymer) error in Ln was similar for all beads and ranged from 8% to 12%. Figure 2 demonstrates quantitative agreement between all-atom (AA) and coarse-grained (CG) density distributions ($\rho_n = \rho_{\text{composite}}(z)/\rho_{\text{melt}}$) for the polymer and sorbitol when using the SC6 bead parameterization. However, a lower water density near the pyrophyllite surface highlights incompatibility between the MARTINI-3 water model and the current CG framework. Furthermore, the average (over amylose and amylopectin) relative percentage error in the near-to-far R_g and S_c ratios was 4.8% and 1.75% for the SC4 bead type, 5.02% and 1.06% for the SC6 bead type, and 6.21% and 3.26% for the SN2 bead

type, respectively. Therefore, it can be concluded that the SC4 and SC6 bead assignments provided satisfactory results for khun segment diffusion, configurational entropy, and density near the pyrophyllite surface. However, we proceeded with the SC6 bead type as our prime choice for subsequent simulations, as its hydration energy showed agreement with results from Lifshitz calculations on experimental surface tension data.

3.2.3 CG Non-bonded Parameters for TMA-MMT Surface

We observed that assigning the uniform SC6 CG bead to all SiO_2 groups on the MMT surface failed to account for localized polarity induced by adjacent highly electronegative oxygen atoms (bonded to octahedral Mg). This simplification resulted in a reduced surface polarity compared to the all-atom (AA) model, leading to a lower sorbitol adsorption on the surface. An iso-surface Electrostatic Potential (ESP) map supports this observation by revealing the most negative surface charge concentrated on the surface oxygen atoms, particularly within the central area of the unit cell where Mg -substitutions are located in the octahedral sheet.⁹⁵ Therefore, we modeled MMT surface SiO_2 with SC6 beads for aluminum-connected sites and tested five higher-polarity bead types (SN6, SP1, SP2, SP4, and SP6) for magnesium-connected SiO_2 sites, optimizing bead assignment to best reproduce the structural, thermodynamic, and dynamic properties of TPS near the surface. We observed that the average relative error (over amylose and amylopectin) w.r.t. AA D_n increased continuously from SN6 to SP6 (11.29% to 29.20%), see Table 3. However, the lower polarity of the SN6 bead allowed the lower accumulation of sorbitol near the TMA-MMT surface, giving a high error in Ar (see Figure S8 for all the data). The relative percentage error (w.r.t. AA) in sorbitol Ar continuously decreased from SN6 (25.50%) to SP6 (5.37%). The observed relative error in Ln was similar for all the parameters and was close to 7%. We found that the SP6 bead assignment most accurately reproduced the AA density profile of sorbitol and polymer (measured Ar) around TMA-MMT, but the least accurate diffusion coefficient (D_n), while SN6 gave the least accurate density profile of sorbitol and polymer and the most

accurate dynamics. However, the SP1 bead gave optimal reproduction of A_r (percent error = 16.49 %) and D_n (percent error = 18.61 %). The other properties like the AA near-to-melt R_g and S_c ratios show good agreement with all CG parameters and the maximum error was less than 7 % (see Table 3).

3.2.4 Validation of Developed Parameters

We used Equation S5 to estimate $S_{2,\alpha,\beta}$, thereby evaluating the robustness of the developed parameters for properties not considered during parameterization. We observed an excellent

Table 4: Normalized two-body excess entropy of TPS-clay composite systems Two-body excess entropies ($S_{2,\alpha,\beta}$) of all polymer-sorbitol pairs within TPS-PY and TPS-TMA–MMT systems were calculated using their respective radial distribution functions (RDF), as shown in Figures S11 and S12. These values were subsequently normalized using $S_{2,\alpha,\beta}$ values of TPS melt (Table S2). Five bonded atoms are excluded from all the calculations. P and S refer to polymer (amylose and amylopectin) and sorbitol beads, respectively.

System	near			far		
	P-P	P-S	S-S	P-P	P-S	S-S
TPS-PY						
AA	1.21	1.44	0.98	0.95	1.30	1.14
CG	1.17	1.33	0.92	0.94	1.23	0.88
TPS-TMA–MMT						
AA	1.29	1.40	1.02	0.91	1.24	1.05
CG	1.24	1.31	0.97	0.98	1.25	0.88

agreement between AA and CG $S_{2,\alpha,\beta}$ for both TPS-PY and TPS-TMA–MMT systems (Table 4). The $S_{2,\alpha,\beta}$ values for polymer-polymer (P-P), polymer-sorbitol (P-S), and sorbitol-sorbitol (S-S) pairs in the near region exhibited low relative errors w.r.t. AA simulations, with pyrophyllite clay showing errors of only 3.25 %, 7.50 %, and 5.50 %, respectively, and TMA–MMT showing errors of 4.05 %, 6.52 %, and 5.24 %, respectively. These results confirm the model’s reliability in predicting properties in large systems that are beyond the reach of AA simulations. Consequently, we used CG models of clay and polymers to investigate the

interfacial and morphological properties of PE-TPS melt and PE-TPS-Cloisite composites.

3.3 TPS-PE and TPS-PE-Cloisite composite

The polymeric chains in these systems surpass their entanglement length, leading to significantly slowed dynamics within the system. Therefore, we have checked the evolution of CN, R_g , and S_c to ensure proper sampling and equilibration of the structures during annealing cycles followed by final runs. We have used the average over 50 ns blocks (making up 100 structures) to investigate the evolution of CN. The high degrees of freedom in polymer chains required a larger block size of 100 ns to correctly estimate S_c and R_g , a block size of 300 ns was used for estimation of amylopectin S_c . The dynamics depicted (see Figure 3 and S9) that all the properties had very high fluctuation during annealing cycles (conducted between 613 K and 913 K), indicating exploration of a large free energy landscape. It was also observed that after annealing cycles, the CN of all the pairs, S_c , and R_g show convergence within the first 600 ns simulation. However, the R_g of PE did not reach a clear plateau, although the standard deviation remained below 3% after 900 ns. Therefore, block averages and errors are reported for the final 900 ns of trajectories, except for PE R_g , which was analyzed using the last 600 ns trajectory.

3.3.1 Morphological Evolution and Density Profiles for TPS-PE and TPS-PE-Cloisite Composite

A small decrease (1 - 3 %) in self-interaction of PE and TPS from the melt to the composite system was observed (Figure 3 (a), (b)) due to the formation of new contacts of polymers with clay. The higher CN of TPS-TPS compared to PE-PE indicates denser local packing of TPS beads, consistent with TPS's relatively higher bulk density. The TPS-PE CN in the composite initially exceeded melt-phase values by $\sim 40\%$ (Figure 3 (c)), subsequently decreasing to converge with melt-equivalent CN. This transient enhancement likely stems from the initial placement of Cloisite-15A clay at the interface, which mediates TPS-PE interac-

tions through its dual functionality. The clay binds TPS primarily via its bare polar surface, as evidenced by the CN profile in Figure 3 (g), where alkyl grafts contribute minimally to clay-TPS adhesion. In contrast, PE adhesion to the clay is governed by alkyl-mediated interactions, as evidenced by the identical clay-clay and clay-PE CN profiles in Figures 3 (e), (f), and (h). Together, these findings illustrate how Cloisite-15A clay facilitates distinct adhesion mechanisms for TPS and PE at the composite interface. The reduction in TPS-PE CN within the composite is directly linked to the interfacial movement of Cloisite-15A clay, as evidenced by two key observations. First, the parallel decrease in clay-TPS CN (Figure 3 (g)) confirms minimal clay migration from the interface. Second, clay-TPS CN remains substantially higher than both clay-clay and clay-PE CN values throughout the simulation, demonstrating persistent localization of Cloisite-15A at the TPS/PE boundary. This interfacial stabilization prevents clay redistribution into the bulk polymer phases, maintaining its role as a compatibilizer despite the gradual convergence of CN. The spatial distribution of clay tactoids at the TPS-PE interface and within the PE bulk exhibits strong agreement with experimental TEM micrographs of composites with equivalent composition.^{28,75} The clay-clay CN indicated a higher surface coverage by alkyl grafts (Figure 3 (d), (e)), making $\approx 70\%$ contribution in self CN from the graft. The high surface coverage and chemical similarity of PE and grafts resulted in comparable clay-clay and clay-PE CN (Figure 3 (e), (f), (h)). However, within the PE bulk, the internal polar surfaces of Cloisite-15A clay drive morphology evolution by promoting clay aggregation, as evidenced by the continuous rise in clay-clay CN (Figure 3 (d)). Over the final 900 ns of the simulation, the average clay-clay CN was approximately three times higher than the clay-PE CN. This pronounced difference indicates the formation of tactoids in the PE bulk, a phenomenon that is consistent with observations from several experimental studies.^{28,75}

The tactoid formation is directly evidenced by a bimodal distribution of clay density within the PE bulk, characterized by two adjacent peaks in the density profile (Figure 5 (b)). Further, the density profiles of individual TPS components—amylose, amylopectin, and sor-

bitol—highlight their distinct interfacial behaviors in the presence and absence of clay (Figure 5). In the TPS-PE melt system, the contrasting chemical nature of TPS and PE leads to flat density profiles at their interface. Among TPS components, linear amylose chains are more strongly repelled by PE than branched amylopectin, resulting in greater amylopectin accumulation at the interface (Figure 5 (a) and (c)). In the composite system, however, amylose preferentially adsorbs to the clay surface, displacing amylopectin from the TPS-clay interface (Figure 5 (b) and (d)). Since amylose and amylopectin share the same monomeric units, these redistributions are primarily driven by entropic interactions. Sorbitol, the most polar TPS constituent, exhibits negligible interfacial accumulation in both melt and composite systems. This contrasts starkly with its strong adsorption at the TPS-TMA-MMT interface (Figure 2 (d)), demonstrating that even minor surface modifications, such as replacing polar TMA with nonpolar alkyl grafts, can radically alter component distribution and morphology. The CG model’s ability to quantitatively capture these polarity-dependent interactions, including fine-grained redistributions across chemically distinct interfaces, validates its utility for application-specific compatibilizer design.

3.3.2 Conformational Properties TPS-PE Melt and TPS-PE-Cl Composite

The R_g of all the polymers increased steadily over time (Figure S9). This behavior is expected, as the initial coordinates generated by Packmol were downscaled, resulting in the polymer chains being compressed at the start of the simulation. As the system relaxed, the chains expanded to reach their equilibrium conformation within the first 600 ns simulation. We did not observe a clear plateau for PE R_g , but the error values were less than 3%. A comparison of polymer conformations showed a decrease in PE’s R_g from 8.24 nm in the melt to 7.41 nm in the composite. In contrast, amylose and amylopectin showed expansion in the composite, with amylose’s R_g increasing from 5.39 nm to 5.88 nm and amylopectin’s from 8.21 nm to 8.48 nm. Further, the ratio of polymer R_g in the near- and far-sheet regions indicated amylose expansion and PE contraction near the surface (see Table 5 for absolute

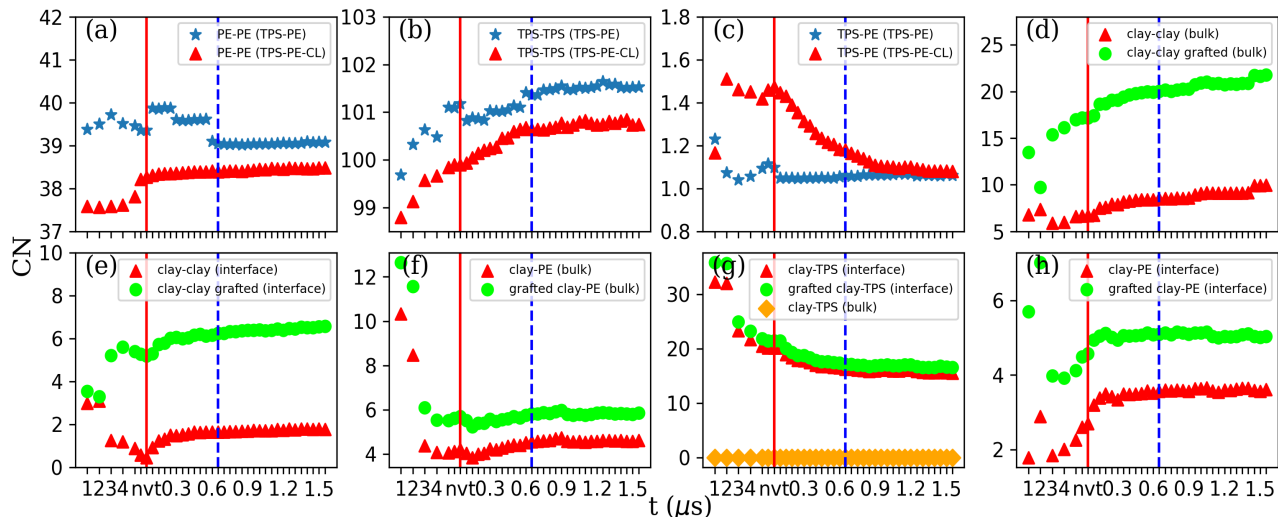


Figure 3: Morphology Evolution in TPS-PE melt and TPS-PE-CL composite systems. The time evolution of second shell coordination number (CN) for various inter- and intra-component pairs in TPS-PE (★) and TPS-PE-CL (▲, ●, ◆) systems. These data are derived from radial distribution functions (RDFs) (Figure S13) obtained from coarse-grained (CG) MARTINI simulations performed at 613K and 1 bar. Panels present CN for: **a** PE-PE, **b** TPS-TPS, **c** TPS-PE, **d** clay-clay (in PE bulk phase), **e** clay-clay (at the TPS-PE interface), **f** clay-TPS (in PE bulk phase), **g** clay-PE (in PE bulk phase), **h** clay-PE (at the TPS-PE interface), and **i** clay-PE (at the TPS-PE interface). The vertical — indicates the annealing period (with results shown against respective cycle number), while - - - denotes the equilibration periods of the simulation.

values). Generally, a polymer’s compaction is linked to repulsive polymer-surface interactions, while its expansion is tied to attractive interactions (see section 3.1 for details). The favorable interaction between amylose and clay clearly agrees with high TPS-clay CN (Figure 3). The comparable clay-clay (at TPS-PE interface) and clay-PE CN indicated neutral, while comparatively higher clay-clay in PE bulk indicated repulsive clay-PE interactions (Figure 3). This observation demonstrates that in multicomponent systems, polymer conformations are governed by the collective interactions (e.g., amylose-clay vs. PE-clay) rather than isolated pairwise interactions, emphasizing the role of competitive adsorption in determining morphology. Therefore, the increase in amylose R_g depicts the relatively favorable, while the decrease in PE R_g indicates the least affinity of PE towards clay. Similarly, preferential absorption of amylose on the clay surface migrated amylopectin away from the surface (Figure 5, giving a lower amylopectin R_g in the near-surface regions. We observed that clay

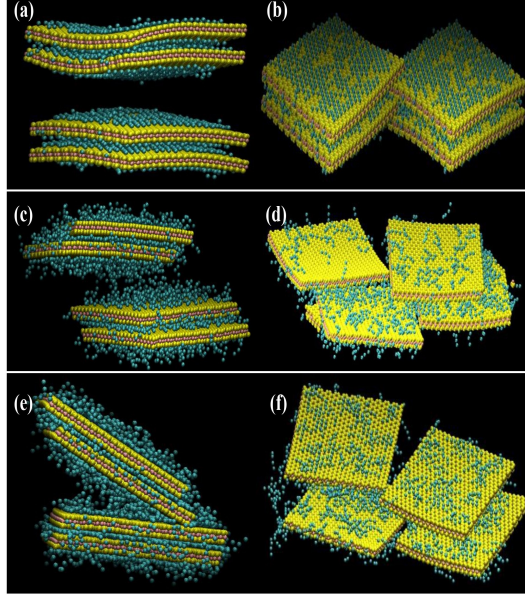


Figure 4: Time evolution of Cloisite-15A clay tactoids in TPS-PE-CL composite system. (a) and (b) show the initial Packmol-generated configurations of clay tactoids in the PE bulk and TPS-PE interface, respectively. (c) and (d) Show the initial configuration for the production runs (obtained after local equilibration), corresponding to the bulk and interfacial clay tactoids, respectively. (e) and (f) display their final structures after 1500 ns of simulation. The alkyl grafts, surface (SC6 and SP2) beads, and the internal (SQ5 and SN4a) beads are represented by cyan, yellow, and pink colors, respectively.

shows a negligible effect on amylopectin and PE S_c , further indicating the entropic nature of interactions. However, a small (3.6 %) decrease observed in amylose S_c is due to favorable amylose-sheet interaction, and the result is consistent with R_g and CN results.

3.3.3 Interfacial Surface Tension of TPS-PE Melt and TPS-PE-Cloisite Composite

The local pressure tensor across a fluid interface is fundamentally linked to the calculation of interfacial tension, as the difference between its normal and tangential components provides a direct mechanical route to quantify surface tension.

In our simulations, we observed that the normal component of the pressure tensor (P_N) remained essentially constant throughout, a stability attributed to the use of the NP_zT ensemble. In contrast, the tangential pressure component (P_T) exhibited significant fluctuations, indicating continuous change in the interfacial interactions. Multiple factors, includ-

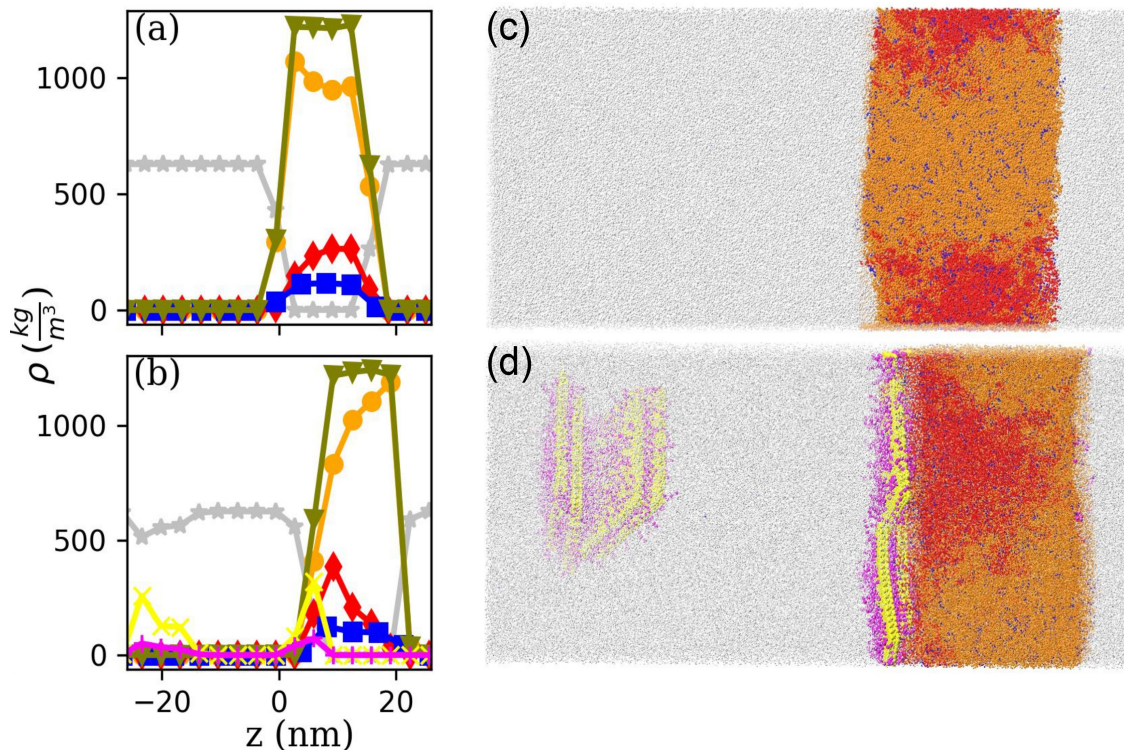


Figure 5: The density profile of of TPS-PE and TPS-PE-CL constituents along the z -axis. **a Density profile of amylose (\blacklozenge), amylopectin (\bullet), polysaccharide (\blacktriangledown), sorbitol (\blacksquare), PE (\blackstar), sheet (\times), and grafts ($+$) in TPS-PE system. **b** Density profile of the same components with additional graft and clay densities in the TPS-PE system. **c** and **d** show the configurations of the TPS-PE melt and TPS-PE-CL composite system, respectively, at the end of the 1500 ns simulation. The color scheme in the snapshot matched their density profiles. All ρ were calculated from the CG MARTINI simulation performed at 613 K and 1 bar**

ing curvature effect and interfacial roughness, drive these changes. Further, the dynamic filler-polymer interactions increased interfacial fluctuations, extending the convergence time to 900 ns in the composite system, compared to 600 ns for the TPS-PE melt. The calculated average γ over converged trajectories of TPS-PE and TPS-PE-CL system were $45 \pm 1.98 \text{ mN m}^{-1}$ and $29 \pm 5.41 \text{ mN m}^{-1}$, respectively. However, the composite system features two distinct types of interfaces: one formed between TPS, PE, and clay components, and another between TPS and PE, which is structurally analogous to the interface in the pure TPS-PE system. To determine the interfacial tension (γ) specific to the TPS-PE-Clay region, the average γ value of the TPS-PE system was used as a reference, resulting in an estimated interfacial tension of 13.06 mN m^{-1} for the TPS-PE-Clay interface. This value is notably lower

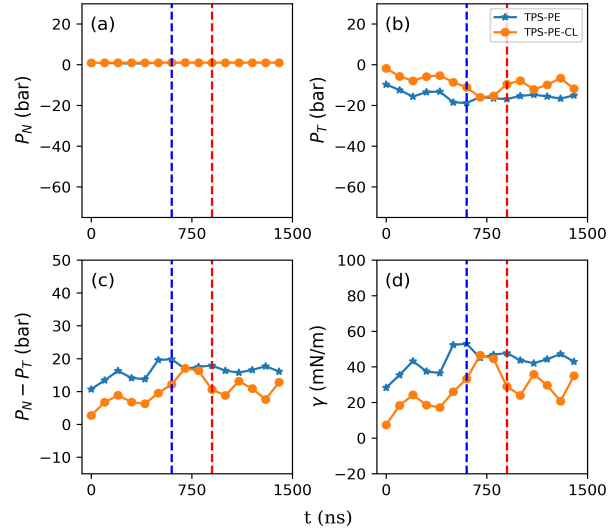


Figure 6: Time-dependent behavior of interfacial properties in TPS-PE melt and TPS-PE-CL composite systems. This Figure presents the time evolution of: **(a)** The normal pressure component (P_N). **(b)** The tangential pressure (P_T) component, calculated as an average of P_{xx} and P_{yy} . **(c)** The pressure anisotropy, determined by the difference between the normal and tangential components ($P_N - P_T$). **(d)** Interfacial surface tension (γ). The data obtained from CG simulation of TPS-PE melt (\star) and TPS-PE-CL (\bullet) systems at 613 K and 100 bar, with each data point showing average property over 100 ns blocks of 1500 ns trajectory.

than that observed in systems without a surface-active component, reflecting the influence of the clay on interfacial properties. The calculation assumes that clay particles present in the bulk do not affect the interfacial properties, an assumption supported by the observed zero contact number (CN) between TPS and bulk clay throughout the simulation (see Figure 3 (g)). These results align with experimental studies, where the addition of Cloisite-15A clay reduces the domain size of TPS from 500 nm to 200 nm in TPS-PE composites,^{28,75} a phenomenon directly attributable to reduced interfacial tension at the polymer-clay interface. The accurate prediction of microscopic properties, as well as capturing macroscopic observation, makes this CG model highly applicable for material design in diverse areas, including paper, packaging, and pharmaceutical industries.

Table 5: Comparison of AA and CG properties in TPS-PE melt and TPS-PE-CL composite system. The average values and error values for interfacial surface tension (γ), configuration entropy per CG bead (S_c), and radius of gyration (R_g) were calculated from the stable regions of the 1500 ns production runs, performed at 613 K and 1 bar. These stable regions are highlighted by **--** in Figure 6 (γ), S10 (S_c), and S9 (R_g), respectively.

	TPS-PE				TPS-PE-CL	
$\gamma(\text{mN m}^{-1})$	45.00 \pm 1.98				29.03 \pm 5.41	
	Amylose		Amylopectin		polyethylene	
	TPS-PE	TPS-PE-CL	TPS-PE	TPS-PE-CL	TPS-PE	TPS-PE-CL
S_c (J mol $^{-1}$ K)	24.21 \pm 0.30	23.33 \pm 0.10	24.28 \pm 0.03	22.34 \pm 0.12	69.29 \pm 0.07	69.64 \pm 0.06
R_g (nm)	5.30 \pm 0.01	5.88 \pm 0.01	8.21 \pm 0.00	8.48 \pm 0.00	8.24 \pm 0.10	7.41 \pm 0.18
	TPS-PE-CL		TPS-PE-CL		TPS-PE-CL	
	near	far	near	far	near	far
R_g (nm)	5.98 \pm 0.09	5.46 \pm 0.05	7.89 \pm 0.21	9.07 \pm 0.24	6.54 \pm 0.11	7.26 \pm 0.09

4 Conclusions

The large molecular weight and slow dynamics of polymers and clay, combined with small time steps in AA simulations, are the major barriers in computational studies of polymer nanocomposite systems. Beyond the general limitations of AA simulations, a significant challenge in applying CG methods, such as Dissipative Particle Dynamics (DPD), to complex systems lies in the prohibitively large and intricate parameter space required for accurately deriving effective interaction potentials. We developed MARTINI CG FF parameters for phyllosilicate clays (pyrophyllite and TMA-MMT) using a combination of Lifshitz theory, experimental surface tension data, and MD simulations. The hydration energy of the pyrophyllite surface, obtained from its surface tension components, quantitatively aligned with the reported value for MARTINI-3 SC6 beads, thus confirming their initial assignment for surface SiO₂. The internal and edge beads were assigned according to standard MARTINI-3 rules, and overall bead combinations were tested against AA properties of solvents and TPS around periodic pyrophyllite clay. The solvent properties (density profiles and diffusion coefficients) around periodic pyrophyllite clay were similar, irrespective of surface bead

type. However, among various surface bead choices (SC4, SC6, SN2, SN4, and SP2) in the TPS-pyrophyllite system, the SC6 bead-type assignment showed optimal reproduction of AA radial distribution function (RDF), TPS polymer density profile around clay (ρ_n), normalized diffusion coefficients of polymer Kuhn segments (D_n), radius of gyration (R_g), conformation entropy (S_c), and two-body excess entropy (S_2). However, the MMT surface representation using a single SC6-type bead CG bead underestimated its polarity, which is induced due to an indirect connectivity with octahedral Mg . This localized nature of the surface agrees with the iso-surface ESP map results, indicating most negative surface charge on the surface oxygen located over Mg -substitutions in the octahedral layer.⁹⁵ Therefore, one-third of surface beads, connected to the Mg site via bridging oxygen, were represented using polar bead (SN6, SP1, SP2, SP4, and SP6). The average (over amylose and amylopectin) relative error w.r.t. AA D_n increased continuously from SN6 to SP6 (11.29% to 29.20%), while the relative percentage error in CG Ar continuously decreased from SN6 to SP6 (25.50% to 5.37%), with the SP1 bead assignment providing optimal values for both properties. Additionally, the SP1 bead assignment gave less than 7% relative error in near-to-melt R_g and S_c ratio of amylose and amylopectin, with minimal error in S_2 ratios for polymer-polymer, polymer-sorbitol, and sorbitol-sorbitol pairs. Additionally, we reported that MARTINI-3 polysaccharide models for amylose and amylopectin overestimated the R_g by $\sim 20\%$ and underestimated S_c by $\sim 8\%$, indicate the need of reparameterization using longer polymeric chains as done in our previous work.³³ Further, the MD simulations of these composite simulations indicated a reduced polymer concentration near the surface accelerated Kuhn segment dynamics in the presence of pyrophyllite, while retarding them with TMA-MMT, relative to the polymer melt. A small decrease in S_c and minimal change in the R_g of these polymers were observed when switching from repulsive pyrophyllite clay to a weakly attractive TMA-MMT surface. The observed behavior of polymer chains was completely different than a typical attractive or repulsive surface, and the interplay of polymer-sheet, sheet-plasticizer, and polymer-plasticizer interaction could be the key reason.

We employed these CG models to perform large-scale simulations that are computationally infeasible with AA simulations, enabling the exploration of system properties and behaviors at significantly larger spatial and temporal scales. We created a phase-separated thermoplastic starch-polyethylene (TPS-PE) melt and its composite (TPS-PE-CL) with commercial Cloisite-15A clay. In the TPS-PE-CL system, one pair of cloisite-15A clay tactoids is at the interface and another in the PE bulk, thus mimicking experimental TPS dispersed PE systems.^{28,75} The coordination number (CN) obtained from these simulations showed that clay compatibilizes TPS-PE by binding TPS through its bare polar surface and PE via alkyl-mediated interactions. This high coordination between TPS-clay increased overall amylose and amylopectin R_g from TPS-PE melt to TPS-PE-CL composite system. Although the clay’s alkyl grafts and the PE matrix exhibited comparable self- and cross-interactions (CN), we observed a decreased polyethylene R_g from TPS-PE melt to TPS-PE-CL composite system. This observation demonstrates that in multicomponent systems, polymer conformations are governed by the collective interactions (e.g., amylose-clay vs. PE-clay) rather than isolated pairwise interactions, emphasizing the role of competitive adsorption in determining morphology. Similarly, preferential absorption of amylose on the clay surface migrated amylopectin away from the surface (Figure 5, giving a lower amylopectin R_g in the near-surface regions. The CN indicated clay tactoid aggregation in the PE bulk, likely caused by internal polar bead interactions within the clay. Further, a significant reduction in interfacial surface tension in TPS-PE melt from 45 mN m^{-1} to 13.06 mN m^{-1} upon Cloisite clay addition, indicating the compatibilization of PE and TPS phase via clay, observation align with observed CN values (Figure 3). The high TPS-clay coordination, persistent localization of clay at the TPS-PE interface, clay aggregation in PE matrix, and reduction in interfacial tension upon clay addition in TPS-PE systems show good agreement with experimental findings.^{28,75} These studies indicated Cloisite-15A clay addition to TPS-PE systems reduced TPS drop size in PE matrix from 500 nm to 200 nm,^{28,75} directly attributable to reduced polymer-clay interfacial tension. Additionally, XRD and TEM studies reported the presence of tactoid

and intercalated clay assemblies within the PE matrix, occupying either the PE bulk or the TPS-PE interface. Our CG model precisely predicted all these crucial material design aspects, thereby establishing a paradigm for time- and cost-effective advancement in novel material development.

Acknowledgement

The author thanks the High-Performance Computing facility of IIT Delhi for providing the resources needed for this work.

References

- (1) Marsh, K.; Bugusu, B. Food packaging - Roles, materials, and environmental issues: Scientific status summary. *Journal of Food Science* **2007**, *72*.
- (2) Babu, R. P.; O’connor, K.; Seeram, R. Current progress on bio-based polymers and their future trends. *Progress in biomaterials* **2013**, *2*, 1–16.
- (3) Jiménez, A.; Fabra, M.; Talens, P.; Chiralt, A. Edible and biodegradable starch films: a review. *Food Bioprocess Technol* *5* (6): 2058–2076. 2012.
- (4) Attaran, S. A.; Hassan, A.; Wahit, M. U. Materials for food packaging applications based on bio-based polymer nanocomposites: A review. *Journal of Thermoplastic Composite Materials* **2017**, *30*, 143–173.
- (5) Carvalho, A. J. Starch: major sources, properties and applications as thermoplastic materials. *Monomers, polymers and composites from renewable resources* **2008**, 321–342.
- (6) Khan, B.; Bilal Khan Niazi, M.; Samin, G.; Jahan, Z. Thermoplastic starch: A possible biodegradable food packaging material—A review. *Journal of Food Process Engineering* **2017**, *40*, e12447.

- (7) Stepto, R. The processing of starch as a thermoplastic. *Macromolecular Symposia*. 2003; pp 203–212.
- (8) de Freitas, A. d. S. M.; da Silva, A. P. B.; Montagna, L. S.; Nogueira, I. A.; Carvalho, N. K.; de Faria, V. S.; Dos Santos, N. B.; Lemes, A. P. Thermoplastic starch nanocomposites: sources, production and applications—a review. *Journal of Biomaterials Science, Polymer Edition* **2022**, *33*, 900–945.
- (9) Kaboorani, A.; Gray, N.; Hamzeh, Y.; Abdulkhani, A.; Shirmohammadli, Y. Tailoring the low-density polyethylene-thermoplastic starch composites using cellulose nanocrystals and compatibilizer. *Polymer Testing* **2021**, *93*, 107007.
- (10) Corrêa, A. C.; de Campos, A.; Claro, P. I. C.; Guimarães, G. G. F.; Mattoso, L. H. C.; Marconcini, J. M. Biodegradability and nutrients release of thermoplastic starch and poly (ϵ -caprolactone) blends for agricultural uses. *Carbohydrate Polymers* **2022**, *282*, 119058.
- (11) Cyras, V. P.; Manfredi, L. B. Physical and mechanical properties of thermoplastic starch / montmorillonite nanocomposite films. **2008**, *73*, 55–63.
- (12) Chocyk, D.; Gladyszewska, B.; Ciupak, A.; Oniszczyk, T.; Moscicki, L.; Rejak, A. Influence of water addition on mechanical properties of thermoplastic starch foils. *International Agrophysics* **2015**, *29*.
- (13) Domene-López, D.; García-Quesada, J. C.; Martín-Gullón, I.; Montalbán, M. G. Influence of starch composition and molecular weight on physicochemical properties of biodegradable films. *Polymers* **2019**, *11*, 1084.
- (14) Salaberria, A. M.; Diaz, R. H.; Labidi, J.; Fernandes, S. C. Role of chitin nanocrystals and nanofibers on physical, mechanical and functional properties in thermoplastic starch films. *Food Hydrocolloids* **2015**, *46*, 93–102.
- (15) Rezaei, M.; Ismail, A. F.; Bakeri, G.; Hashemifard, S. A.; Matsuura, T. Effect of general montmorillonite and Cloisite 15A on structural parameters and performance of mixed matrix membranes contactor for CO₂ absorption. *Chemical Engineering Journal* **2015**,

260, 875–885.

- (16) Zhou, M.; Xu, D. Starch-MMT composite films: Effects of bio-inspired modification on MMT. *Starch-Stärke* **2015**, *67*, 470–477.
- (17) Suter, J. L.; Groen, D.; Coveney, P. V. Chemically specific multiscale modeling of clay-polymer nanocomposites reveals intercalation dynamics, tactoid self-assembly and emergent materials properties. *Advanced Materials* **2015**, *27*, 966–984.
- (18) Altayan, M. M.; Al Darouich, T. Toward reducing the food packaging waste impact: a study on the effect of Starch type and PE type in thermoplastic starch-polyethylene blends. *Chemical Papers* **2022**, *76*, 2447–2457.
- (19) Baumberger, S.; Lapierre, C.; Monties, B.; Della Valle, G. Use of kraft lignin as filler for starch films. *Polymer Degradation and Stability* **1998**, *59*, 273–277.
- (20) Wang, H.; Dong, W.; Li, Y. Compatibilization of Immiscible Polymer Blends Using in Situ Formed Janus Nanomicelles by Reactive Blending. **2015**,
- (21) Mao, C.; Zhu, Y.; Jiang, W. Design of electrical conductive composites: Tuning the morphology to improve the electrical properties of graphene filled immiscible polymer blends. *ACS Applied Materials and Interfaces* **2012**, *4*, 5281–5286.
- (22) Eastwood, E. A.; Dadmun, M. D. Multiblock copolymers in the compatibilization of polystyrene and poly(methyl methacrylate) blends: Role of polymer architecture. *Macromolecules* **2002**, *35*, 5069–5077.
- (23) Huang, M. F.; Yu, J. G.; Ma, X. F. Studies on the properties of Montmorillonite-reinforced thermoplastic starch composites. *Polymer* **2004**, *45*, 7017–7023.
- (24) Krishnamoorti, R.; Vaia, R. A.; Giannelis, E. P. Structure and dynamics of polymer-layered silicate nanocomposites. *Chemistry of Materials* **1996**, *8*, 1728–1734.
- (25) Bher, A.; Unalan, I. U.; Auras, R.; Rubino, M.; Schvezov, C. E. Graphene modifies the biodegradation of poly(lactic acid)-thermoplastic cassava starch reactive blend films. *Polymer Degradation and Stability* **2019**, *164*, 187–197.
- (26) Dutta, R. C.; Bhatia, S. K. Transport Diffusion of Light Gases in Polyethylene Using

- Atomistic Simulations. **2017**,
- (27) Sabetzadeh, M.; Bagheri, R.; Masoomi, M. Effect of nanoclay on the properties of low density polyethylene/linear low density polyethylene/thermoplastic starch blend films. *Carbohydrate Polymers* **2016**, *141*, 75–81.
- (28) Sharif, A.; Aalaie, J.; Shariatpanahi, H.; Hosseinkhanli, H.; Khoshniyat, A. Study on the structure and properties of nanocomposites based on high-density polyethylene/starch blends. *Journal of Polymer Research* **2011**, *18*, 1955–1969.
- (29) Huang, F.; Zhou, S. Molecular Dynamics Simulation of Coiled Carbon Nanotube Pull-Out from Matrix. *International Journal of Molecular Sciences* **2022**, *23*, 9254.
- (30) Guo, L.; Xu, H.; Wu, N.; Yuan, S.; Zhou, L.; Wang, D.; Wang, L. Molecular dynamics simulation of the effect of the thermal and mechanical properties of addition liquid silicone rubber modified by carbon nanotubes with different radii. *e-Polymers* **2023**, *23*, 20228105.
- (31) Lin, K.; Wang, Z. Multiscale mechanics and molecular dynamics simulations of the durability of fiber-reinforced polymer composites. *Communications Materials* **2023**, *4*, 66.
- (32) Gartner III, T. E.; Jayaraman, A. Modeling and simulations of polymers: a roadmap. *Macromolecules* **2019**, *52*, 755–786.
- (33) Patidar, A.; Goel, G. MARTINI Coarse-Grained Force Field for Thermoplastic Starch Nanocomposites. *The Journal of Physical Chemistry B* **2024**,
- (34) Özeren, H. D.; Olsson, R. T.; Nilsson, F.; Hedenqvist, M. S. Prediction of plasticization in a real biopolymer system (starch) using molecular dynamics simulations. *Materials & Design* **2020**, *187*, 108387.
- (35) Panizon, E.; Boicchio, D.; Monticelli, L.; Rossi, G. MARTINI coarse-grained models of polyethylene and polypropylene. *The Journal of Physical Chemistry B* **2015**, *119*, 8209–8216.
- (36) Khan, P.; Goel, G. Martini Coarse-Grained Model for Clay-Polymer Nanocomposites.

Journal of Physical Chemistry B **2019**, *123*, 9011–9023.

- (37) Groot, R. D.; Warren, P. B. Dissipative particle dynamics: Bridging the gap between atomistic and mesoscopic simulation. *Journal of Chemical Physics* **1997**, *107*, 4423–4435.
- (38) Singh, A.; Chakraborti, A.; Singh, A. Role of a polymeric component in the phase separation of ternary fluid mixtures: A dissipative particle dynamics study. *Soft Matter* **2018**, *14*, 4317–4326.
- (39) Fu, Y.; Liao, L.; Yang, L.; Lan, Y.; Mei, L.; Liu, Y.; Hu, S. Molecular dynamics and dissipative particle dynamics simulations for prediction of miscibility in polyethylene terephthalate/polylactide blends. *Molecular Simulation* **2013**, *39*, 415–422.
- (40) Scocchi, G.; Posocco, P.; Fermeglia, M.; Pricl, S. Polymer - Clay nanocomposites: A multiscale molecular modeling approach. *Journal of Physical Chemistry B* **2007**, *111*, 2143–2151.
- (41) Long, D.; Sotta, P. Nonlinear and plastic behavior of soft thermoplastic and filled elastomers studied by dissipative particle dynamics. *Macromolecules* **2006**, *39*, 6282–6297.
- (42) Sliozberg, Y. R.; Gair Jr, J. L.; Hsieh, A. J. Dissipative particle dynamics simulation of microphase separation in polyurethane urea nanocomposites. *Polymer* **2020**, *193*, 122339.
- (43) Khani, S.; Jamali, S.; Boromand, A.; Hore, M. J.; Maia, J. Polymer-mediated nanorod self-assembly predicted by dissipative particle dynamics simulations. *Soft Matter* **2015**, *11*, 6881–6892.
- (44) Wang, J.; Han, Y.; Xu, Z.; Yang, X.; Ramakrishna, S.; Liu, Y. Dissipative particle dynamics simulation: A review on investigating mesoscale properties of polymer systems. *Macromolecular Materials and Engineering* **2021**, *306*, 2000724.
- (45) Ju, S.-P.; Wang, Y.-C.; Huang, G.-J.; Chang, J.-W. Miscibility of graphene and poly(methyl methacrylate)(PMMA): molecular dynamics and dissipative particle dynamics

- simulations. *Rsc Advances* **2013**, *3*, 8298–8307.
- (46) Schweizer, K. S.; Honnell, K. G.; Curro, J. G. Reference interaction site model theory of polymeric liquids: Self-consistent formulation and nonideality effects in dense solutions and melts. *The Journal of chemical physics* **1992**, *96*, 3211–3225.
- (47) Schweizer, K. S.; Fuchs, M.; Szamel, G.; Guenza, M.; Tang, H. Polymer-mode-coupling theory of the slow dynamics of entangled macromolecular fluids. *Macromolecular theory and simulations* **1997**, *6*, 1037–1117.
- (48) Zirkel, A.; Gruner, S.; Urban, V.; Thiyagarajan, P. Small-angle neutron scattering investigation of the Q-dependence of the Flory- Huggins interaction parameter in a binary polymer blend. *Macromolecules* **2002**, *35*, 7375–7386.
- (49) Wu, J. Density functional theory for chemical engineering: From capillarity to soft materials. *AIChE journal* **2006**, *52*, 1169–1193.
- (50) Oxtoby, D. W. Density functional methods in the statistical mechanics of materials. *Annual Review of Materials Research* **2002**, *32*, 39.
- (51) Helfand, E.; Sapse, A. M. Theory of unsymmetric polymer–polymer interfaces. *The Journal of chemical physics* **1975**, *62*, 1327–1331.
- (52) Helfand, E.; Wasserman, Z. R. Block copolymer theory. 4. Narrow interphase approximation. *Macromolecules* **1976**, *9*, 879–888.
- (53) Lowden, L. J.; Chandler, D. Solution of a new integral equation for pair correlation functions in molecular liquids. *The Journal of Chemical Physics* **1973**, *59*, 6587–6595.
- (54) Sung, B. J.; Yethiraj, A. Integral equation theory of randomly coupled multiblock copolymer melts: Effect of block size on the phase behavior. *The Journal of chemical physics* **2005**, *123*, 214901.
- (55) Hall, L. M.; Schweizer, K. S. Impact of monomer sequence, composition and chemical heterogeneity on copolymer-mediated effective interactions between nanoparticles in melts. *Macromolecules* **2011**, *44*, 3149–3160.
- (56) Martin, T. B.; Jayaraman, A. Using theory and simulations to calculate effective

- interactions in polymer nanocomposites with polymer-grafted nanoparticles. *Macromolecules* **2016**, *49*, 9684–9692.
- (57) Hsu, C.; Chandler, D. RISM calculation of the structure of liquid chloroform. *Molecular Physics* **1979**, *37*, 299–301.
- (58) Martin, T. B.; Gartner III, T. E.; Jones, R. L.; Snyder, C. R.; Jayaraman, A. pyPRISM: a computational tool for liquid-state theory calculations of macromolecular materials. *Macromolecules* **2018**, *51*, 2906–2922.
- (59) Reith, D.; Meyer, H.; Müller-Plathe, F. Mapping atomistic to coarse-grained polymer models using automatic simplex optimization to fit structural properties. *Macromolecules* **2001**, *34*, 2335–2345.
- (60) Reith, D.; Pütz, M.; Müller-Plathe, F. Deriving effective mesoscale potentials from atomistic simulations. *Journal of computational chemistry* **2003**, *24*, 1624–1636.
- (61) Izvekov, S.; Voth, G. A. A multiscale coarse-graining method for biomolecular systems. *The Journal of Physical Chemistry B* **2005**, *109*, 2469–2473.
- (62) Marrink, S. J.; Risselada, H. J.; Yefimov, S.; Tieleman, D. P.; De Vries, A. H. The MARTINI force field: Coarse grained model for biomolecular simulations. *Journal of Physical Chemistry B* **2007**, *111*, 7812–7824.
- (63) Moore, T. C.; Iacovella, C. R.; McCabe, C. Derivation of coarse-grained potentials via multistate iterative Boltzmann inversion. *The Journal of chemical physics* **2014**, *140*.
- (64) Ndao, M.; Devémy, J.; Ghoufi, A.; Malfreyt, P. Coarse-graining the liquid–liquid interfaces with the MARTINI force field: How is the interfacial tension reproduced? *Journal of chemical theory and computation* **2015**, *11*, 3818–3828.
- (65) López, C. A.; Rzepiela, A. J.; de Vries, A. H.; Dijkhuizen, L.; Hünenberger, P. H.; Marrink, S. J. Martini coarse-grained force field: Extension to carbohydrates. *Journal of Chemical Theory and Computation* **2009**, *5*, 3195–3210.
- (66) Wu, D.; Yang, X. Coarse-grained molecular simulation of self-assembly for nonionic surfactants on graphene nanostructures. *The Journal of Physical Chemistry B* **2012**,

116, 12048–12056.

- (67) Gobbo, C.; Beurroies, I.; de Ridder, D.; Eelkema, R.; Marrink, S. J.; De Feyter, S.; van Esch, J. H.; de Vries, A. H. MARTINI model for physisorption of organic molecules on graphite. *The Journal of Physical Chemistry C* **2013**, *117*, 15623–15631.
- (68) Piskorz, T. K.; Gobbo, C.; Marrink, S. J.; De Feyter, S.; De Vries, A. H.; Van Esch, J. H. Nucleation mechanisms of self-assembled physisorbed monolayers on graphite. *The Journal of Physical Chemistry C* **2019**, *123*, 17510–17520.
- (69) Sukenik, S.; Sapir, L.; Harries, D. Osmolyte induced changes in peptide conformational ensemble correlate with slower amyloid aggregation: a coarse-grained simulation study. *Journal of Chemical Theory and Computation* **2015**, *11*, 5918–5928.
- (70) Schmalhorst, P. S.; Deluweit, F.; Scherrers, R.; Heisenberg, C. P.; Sikora, M. Overcoming the Limitations of the MARTINI Force Field in Simulations of Polysaccharides. *Journal of Chemical Theory and Computation* **2017**, *13*, 5039–5053.
- (71) Shivgan, A. T.; Marzinek, J. K.; Huber, R. G.; Krah, A.; Henchman, R. H.; Matsu-daira, P.; Verma, C. S.; Bond, P. J. Extending the Martini coarse-grained force field to N-Glycans. *Journal of Chemical Information and Modeling* **2020**, *60*, 3864–3883.
- (72) Souza, P. C.; Alessandri, R.; Barnoud, J.; Thallmair, S.; Faustino, I.; Grünewald, F.; Patmanidis, I.; Abdizadeh, H.; Bruininks, B. M.; Wassenaar, T. A.; others Martini 3: a general purpose force field for coarse-grained molecular dynamics. *Nature methods* **2021**, *18*, 382–388.
- (73) Lutsyk, V.; Wolski, P.; Plazinski, W. Extending the Martini 3 coarse-grained force field to carbohydrates. *Journal of Chemical Theory and Computation* **2022**, *18*, 5089–5107.
- (74) Grünewald, F.; Alessandri, R.; Kroon, P. C.; Monticelli, L.; Souza, P. C.; Marrink, S. J. Polyply; a python suite for facilitating simulations of macromolecules and nanomaterials. *Nature communications* **2022**, *13*, 68.
- (75) Sabetzadeh, M.; Bagheri, R.; Masoomi, M. Effect of nanoclay on the properties of low density polyethylene/linear low density polyethylene/thermoplastic starch blend films.

- Carbohydrate Polymers* **2016**, *141*, 75–81.
- (76) Jo, S.; Kim, T.; Iyer, V. G.; Im, W. CHARMM-GUI: a web-based graphical user interface for CHARMM. *Journal of computational chemistry* **2008**, *29*, 1859–1865.
- (77) Guvench, O.; Mallajosyula, S.; Raman, E.; Hatcher, E.; Vanommeslaeghe, K.; Foster, T.; Jamison, F. II and Mackerell AD Jr (2011) CHARMM additive all-atom force field for carbohydrate derivatives and its utility in polysaccharide and carbohydrate-protein modeling. *J Chem Theory Comput* **7**, 3162–3180.
- (78) Guvench, O.; Hatcher, E.; Venable, R. M.; Pastor, R. W.; MacKerell Jr, A. D. CHARMM additive all-atom force field for glycosidic linkages between hexopyranoses. *Journal of chemical theory and computation* **2009**, *5*, 2353–2370.
- (79) Heinz, H.; Koerner, H.; Anderson, K. L.; Vaia, R. A.; Farmer, B. Force field for mica-type silicates and dynamics of octadecylammonium chains grafted to montmorillonite. *Chemistry of materials* **2005**, *17*, 5658–5669.
- (80) Martínez, L.; Andrade, R.; Birgin, E. G.; Martínez, J. M. PACKMOL: a package for building initial configurations for molecular dynamics simulations. *Journal of computational chemistry* **2009**, *30*, 2157–2164.
- (81) Abraham, M. J.; Murtola, T.; Schulz, R.; Páll, S.; Smith, J. C.; Hess, B.; Lindahl, E. GROMACS: High performance molecular simulations through multi-level parallelism from laptops to supercomputers. *SoftwareX* **2015**, *1*, 19–25.
- (82) Churakov, S. V. Ab initio study of sorption on pyrophyllite: Structure and acidity of the edge sites. *The Journal of Physical Chemistry B* **2006**, *110*, 4135–4146.
- (83) Giese, R.; Costanzo, P.; Van Oss, C. The surface free energies of talc and pyrophyllite. *Physics and Chemistry of Minerals* **1991**, *17*, 611–616.
- (84) Sabetzadeh, M.; Bagheri, R.; Masoomi, M. Effect of nanoclay on the properties of low density polyethylene/linear low density polyethylene/thermoplastic starch blend films. *Carbohydrate polymers* **2016**, *141*, 75–81.
- (85) Sharma, R.; Agarwal, M.; Chakravarty, C. Estimating the entropy of liquids from

- atom–atom radial distribution functions: Silica, beryllium fluoride and water. *Molecular Physics* **2008**, *106*, 1925–1938.
- (86) Schlitter, J. Estimation of absolute and relative entropies of macromolecules using the covariance matrix. *Chemical physics letters* **1993**, *215*, 617–621.
- (87) Kirkwood, J. G.; Buff, F. P.; Green, M. S. The statistical mechanical theory of transport processes. III. The coefficients of shear and bulk viscosity of liquids. *The Journal of Chemical Physics* **1949**, *17*, 988–994.
- (88) Park, H.-M.; Li, X.; Jin, C.-Z.; Park, C.-Y.; Cho, W.-J.; Ha, C.-S. Preparation and properties of biodegradable thermoplastic starch/clay hybrids. *Macromolecular Materials and Engineering* **2002**, *287*, 553–558.
- (89) Suter, J. L.; Coveney, P. V. Computer simulation study of the materials properties of intercalated and exfoliated poly (ethylene) glycol clay nanocomposites. *Soft Matter* **2009**, *5*, 2239–2251.
- (90) Smith, G. D.; Bedrov, D.; Li, L.; Bytner, O. A molecular dynamics simulation study of the viscoelastic properties of polymer nanocomposites. *The Journal of chemical physics* **2002**, *117*, 9478–9489.
- (91) Varnik, F.; Baschnagel, J.; Binder, K. Reduction of the glass transition temperature in polymer films: A molecular-dynamics study. *Physical Review E* **2002**, *65*, 021507.
- (92) Müller, C. M.; Laurindo, J. B.; Yamashita, F. Composites of thermoplastic starch and nanoclays produced by extrusion and thermopressing. *Carbohydrate polymers* **2012**, *89*, 504–510.
- (93) Schlemmer, D.; Angélica, R. S.; Sales, M. J. A. Morphological and thermomechanical characterization of thermoplastic starch/montmorillonite nanocomposites. *Composite Structures* **2010**, *92*, 2066–2070.
- (94) Soni, J.; Gupta, S.; Mandal, T. Recalibration of MARTINI-3 Parameters for Improved Interactions between Peripheral Proteins and Lipid Bilayers. *Journal of Chemical Theory and Computation* **2024**, *20*, 9673–9686.

- (95) Lavikainen, L. P.; Tanskanen, J. T.; Schatz, T.; Kasa, S.; Pakkanen, T. A. Montmorillonite interlayer surface chemistry: effect of magnesium ion substitution on cation adsorption. *Theoretical Chemistry Accounts* **2015**, *134*, 1–7.

5 Supplementary Material

5.1 Temperature-pressure annealing cycles

Preparing the Equilibrated TPS Structure We prepared an equilibrated Thermoplastic Starch (TPS) structure, free from the memory effects of its initial configuration, through a multi-step simulation process. We began by generating an initial simulation box using the Packmol software. To achieve a dense, equilibrated system, we first incrementally rescaled the coordinates of the simulation box by 29.17 nm^3 , performing energy minimization with the steepest descent algorithm after each step. Following this density increase, we applied temperature-pressure (T-P) annealing cycles to the rescaled TPS system (referred to as "state A"). This was crucial for accelerating the slow dynamics inherent to starch chains, allowing the system to reach an equilibrated configuration more rapidly. During these cycles, we carefully controlled the temperature, ensuring simulation times at both lower and higher temperatures (613 K) to achieve local equilibration (evidenced by a potential energy plateau) and Brownian relaxation of the polymer chains (Figure S1 (A)). After each temperature cycle, we incrementally doubled the pressure up to 1000 bar, subsequently depressurizing back to 1 bar using the same stepwise approach (Figure S1 (C)). This entire T-P cycling process was repeated until the densities of the initial (state A) and final (state A') states converged, confirming the attainment of an equilibrated structure (Figure S1 (C)).

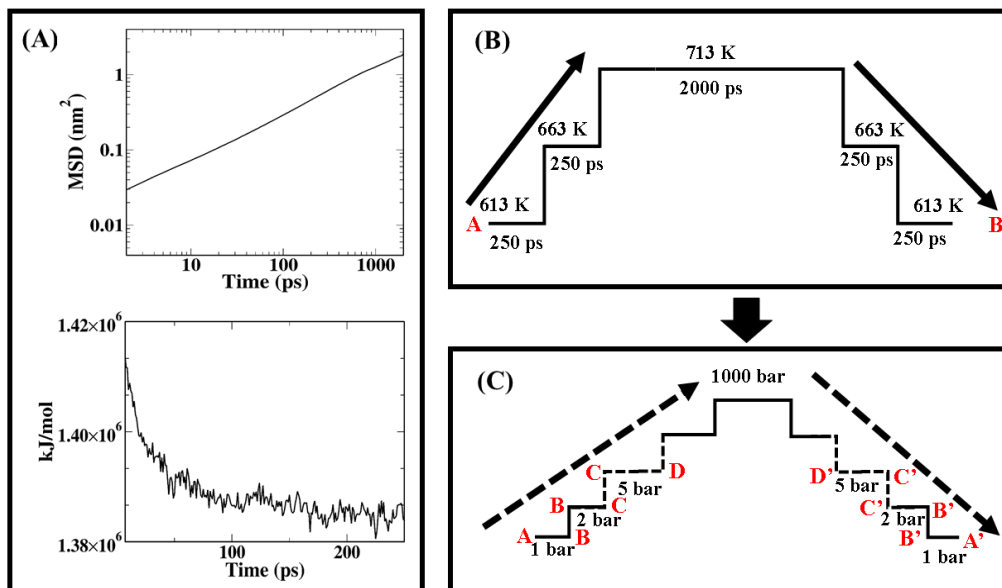


Figure S1: Temperature-pressure annealing simulations, The temperature cycle (B) was performed on the rescaled simulation box (state A). The figure shows the simulation time and temperature at each step. These temperature cycles were performed at various pressure values indicated in (B). The simulation time at higher (713 K) and lower (613 K) temperature is based mean-square displacement (at 713 K) and potential energy (at 613 K) (shown in A), respectively.

5.2 AA and CG Structures

This section presents Atomistic (AA) and Coarse-Grained (CG) representations of key systems simulated in this study.

5.3 Calculation of surface hydration energies

We used the Equation S1 over the contact angle of α -bromonaphthalene (38.7°) and diiodomethane (51.1°) on pyrophyllite clay to estimate the dispersive lifshitz component (γ_s^{LW}) of pyrophyllite clay. The values of γ_l^{LW} of α -bromonaphthalene and diiodomethane were available in the literature and were 44.4 mN m^{-1} and 50.8 mN m^{-1} , respectively.⁸³

$$(1 + \cos\theta)\gamma_l = 2(\sqrt{\gamma_l^{LW}\gamma_s^{LW}}) + \sqrt{\gamma_l^+\gamma_s^-} + \sqrt{\gamma_l^-\gamma_s^+} \quad (\text{S1})$$

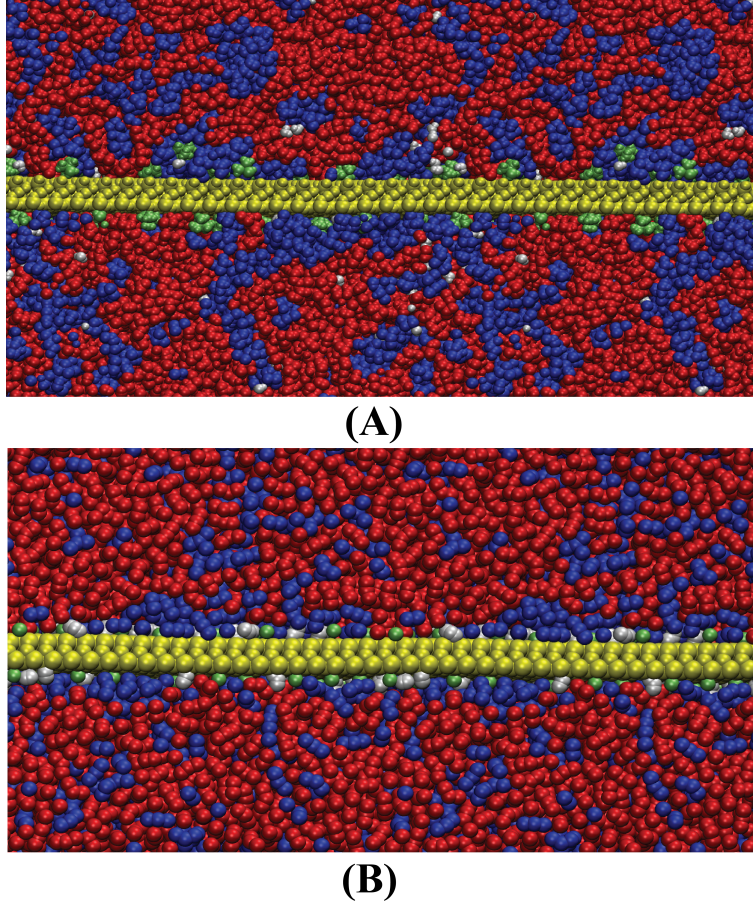


Figure S2: AA and CG representation of TPS-TMA-MMT composite system. (a) shows the AA representation of the TPS-TMA-MMT composite system. (b) shows the same system in CG representation. The polymer (red), sorbitol (blue), water (white), sheet (yellow), and TMA ion (lime) beads are represented by different colors.

The γ_s^- , γ_s^+ , γ_l^- , and γ_l^+ are the donor and acceptor contribution solid and liquid polar component (γ_i^{AB} or γ_s^{AB}), respectively (see Equation S2).

$$\gamma_i^{AB} = 2\sqrt{\gamma_i^- \gamma_i^+} \quad (\text{S2})$$

The γ_l^- and γ_l^+ is zero for these two liquids, making γ_l^{LW} and γ_l equal. We obtained γ_s^{LW} of 35.19 mN m^{-1} and 33.67 mN m^{-1} from the data of these two liquids. Therefore, we have taken an average γ_s^{LW} (34.4 mN m^{-1}) of these two liquids for the other calculations. The values of the water and ethylene glycol contact angles over pyrophyllite surface (72.8° and 48°), γ_l^- (25.5 and 1.92 mN m^{-1}), and γ_l^+ (25.5 and 47 mN m^{-1}) were integrated in Equation S1 to

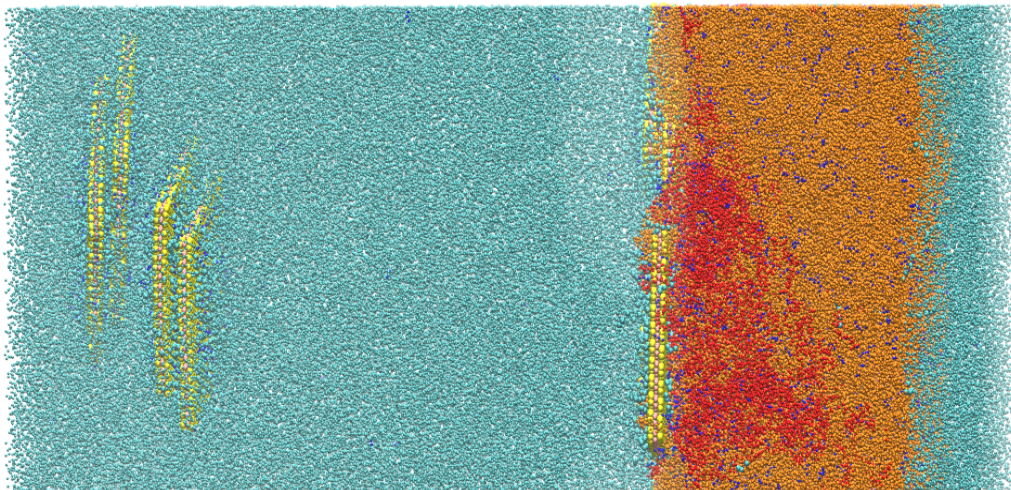


Figure S3: TPS-PE-CL system The equilibrated morphology of TPS-PE-CL system obtained at the end of temperature-pressure annealing cycles. The Cloisite surface SiO_2 , internal MgOH_2 or AlOH_2 , and graft (C16 alkyl chains) CG beads are represented by yellow, pink, and cyan colors, respectively. The amylose, amylopectin, and sorbitol CG beads are represented by red, orange, and blue colors, respectively.

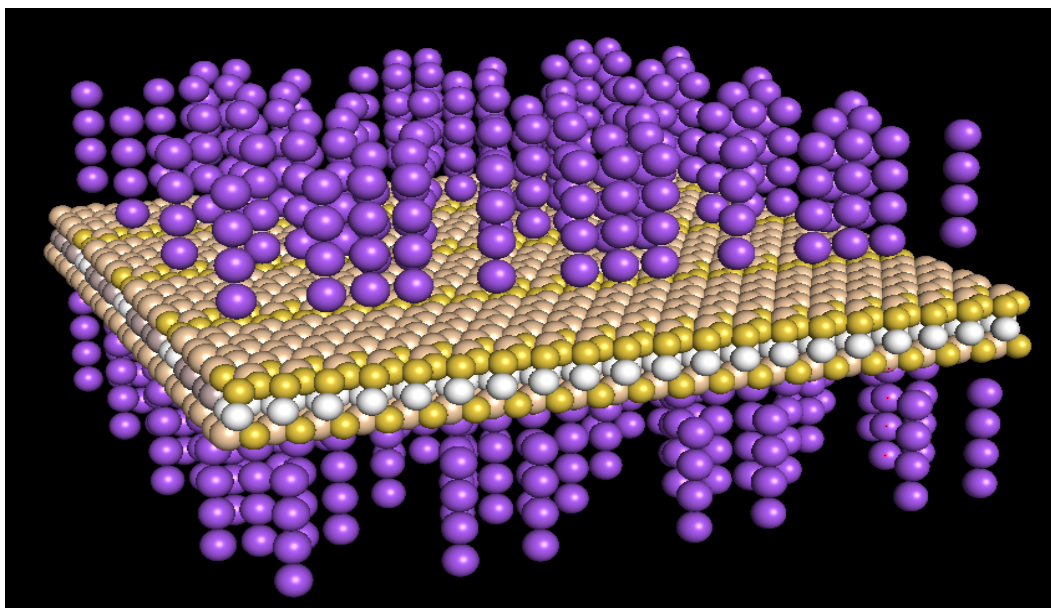


Figure S4: Structure of cloisite 15-A sheet The C16 graft, depicted as four blue CG beads (shown in blue), was grown on the MMT sheet by leveraging the TMA positions within a well-equilibrated TMA-MMT structure. The surface and internal beads of the sheet are represented by yellow and white colors, respectively.

calculate γ_s^+ (3.2 mN m^{-1}) and γ_s^- (1.7 mN m^{-1}). Further, the values of polar and dispersive components of water and pyrophyllite were integrated into Equation S3 to calculate hydration

energy ($\Delta F_{hydration}$) of the pyrophyllite surface.

$$\Delta F_{hydration} = (-2\gamma_l^{LW} + 4\sqrt{\gamma_l^{LW}\gamma_s^{LW}}) - (2\gamma_l^{AB} + 4\sqrt{\gamma_l^+\gamma_s^-} + 4\sqrt{\gamma_l^-\gamma_s^+}) \quad (S3)$$

The calculated $\Delta F_{hydration}$ (2.31 kJ mol⁻¹) cannot be directly compared to the hydration energies of the MARTINI-3 CG beads, as the force field captures only relative trends rather than absolute hydration energy values. Therefore, we used Equation S4 to extrapolate experimental $\Delta F_{hydration}$ to the simulation $\Delta F_{hydration}$. The equation was obtained by fitting the experimental and simulation hydration energies of thirty-six organic liquids of various polarities, and reported in the recent MARTINI-3 work.⁷²

$$y = 0.65x - 4.52 \quad (S4)$$

, Where y and x represent the hydration energies of various polarity liquids using CG simulation and experiments, respectively. The calculated hydration value (-1.65 kJ mol⁻¹) is in close agreement with SC6 beads (-2.00 kJ mol⁻¹),⁷² and the choice seems reasonable, as pyrophyllite clay has a nonpolar nature.⁸³

5.4 Key Results

$$S_{2,\alpha\beta} = -\pi\rho \int_0^\infty g_{\alpha\beta}(r)\ln g_{\alpha\beta}(r) - [g_{\alpha\beta}(r) - 1]rdr \quad (S5)$$

The center of mass positions of functional groups (corresponding to CG beads) in AA trajectories were converted to pseudo-CG trajectories using Equation S6.

$$r_i^{CG} = \frac{\sum_{j=1}^n r_j m_j}{\sum_{j=1}^n m_j} \quad (S6)$$

Where, m_j and r_i are the masses and positions of atoms, r_i^{CG} are the positions for pseudo-CG

Table S1: Comparison of AA and CG normalized diffusion coefficients for five solvents in pyrophyllite-solvent systems The normalized diffusion coefficients (D_n) for each solvent were calculated using different CG bead assignments for surface SiO_2 . All simulations were performed at 300 K and 1 bar.

Solvent	Hexadecane	1-Propanol	Ethanol	Iso-Propanol	Sorbitol
AA	2.19	1.42	1.32	1.44	1.62
CG bead type	C6	N6	SP1	P1	P4
SC4	0.64	0.87	0.98	0.87	0.91
SC6	0.70	0.83	0.98	0.83	0.81
SN2	0.68	0.81	0.98	0.81	0.80
SN4	0.71	0.79	0.95	0.79	0.83
SN6	0.69	0.81	0.95	0.81	0.81
SP2	0.71	0.81	0.97	0.81	0.82

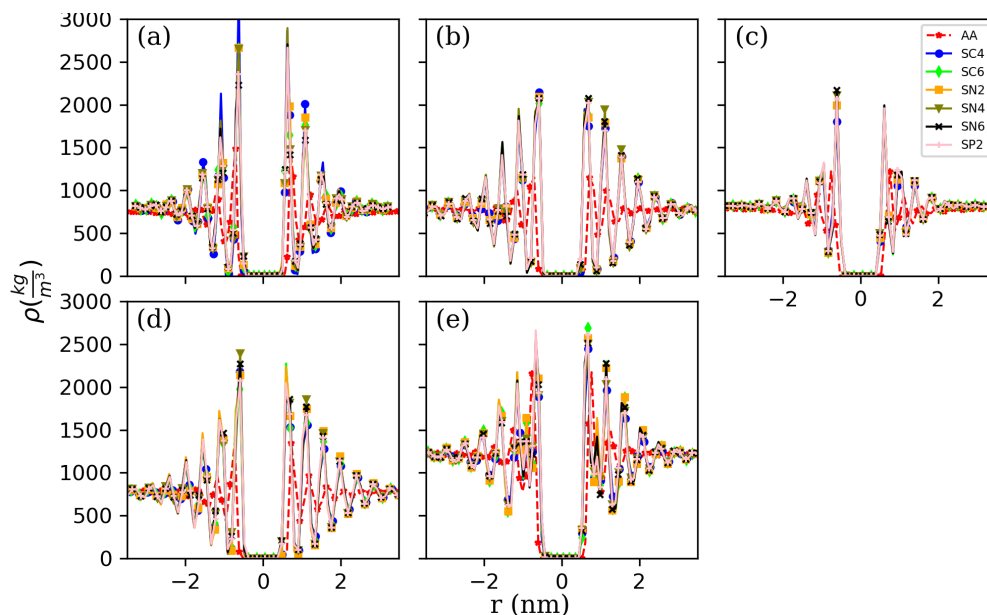


Figure S5: Density profile of small solvent molecules along the z-direction of pyrophyllite clay. (a) Hexadecane, (b) propanol, (c) ethanol, and (d) iso-propanol density profile along the z-direction of pyrophyllite plane were estimated at 300 K and 1 bar. (e) sorbitol density was estimated at 450 K and 1 bar. The CG simulations were performed with different CG bead assignments for surface SiO_2 . The data is shown for SC4 (●), SC6 (▲), SN2 (■), SN4 (▼), SN6 (✕), and SP2 (+) bead assignments, and were plotted along with AA (★) results at the same operating conditions.

beads.

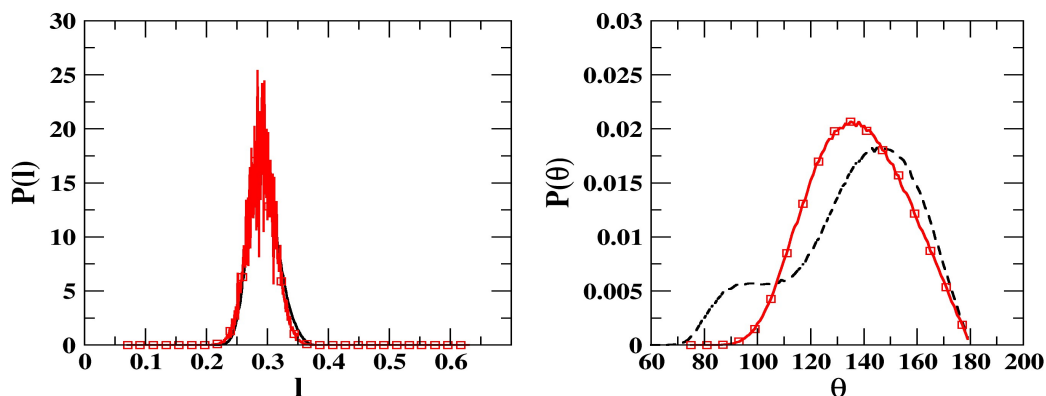


Figure S6: Bonded distributions of sorbitol in AA and CG MARTINI-3 simulations. (a) The bond, and **(b)** angle distribution of sorbitol, both obtained from the AA (---) and CG MARTINI-3 (—□) simulations of TPS melt at 613K.

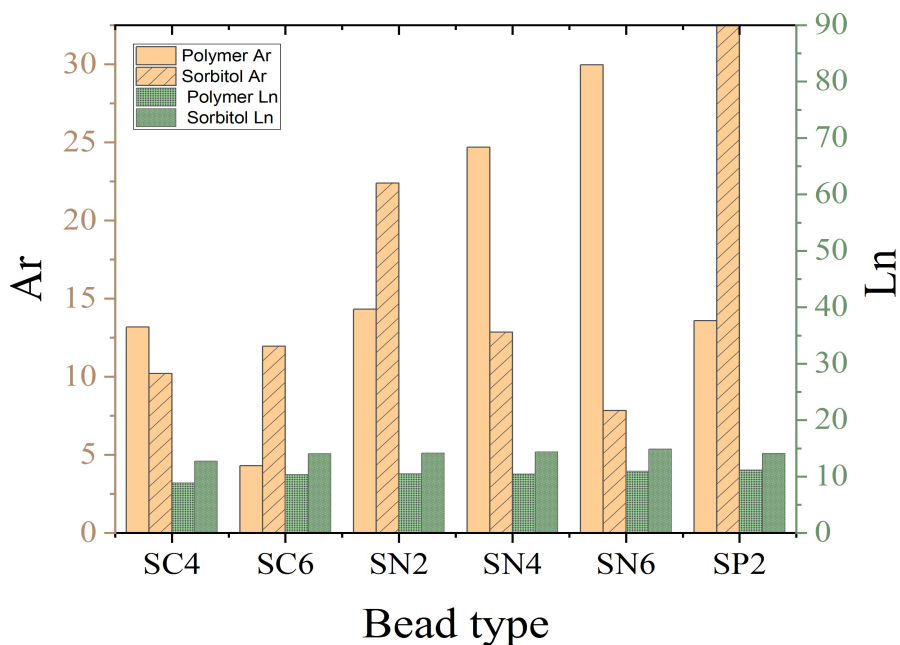


Figure S7: Relative error in CG density profiles of TPS constituents for TPS-PY composite The Ar and Ln were calculated using density profile integrals using Equations 2 and 3, respectively. The integration was performed till the end of the first solvation shell (1 nm). The left and right axes show relative percentage error in Ar and Ln, respectively.

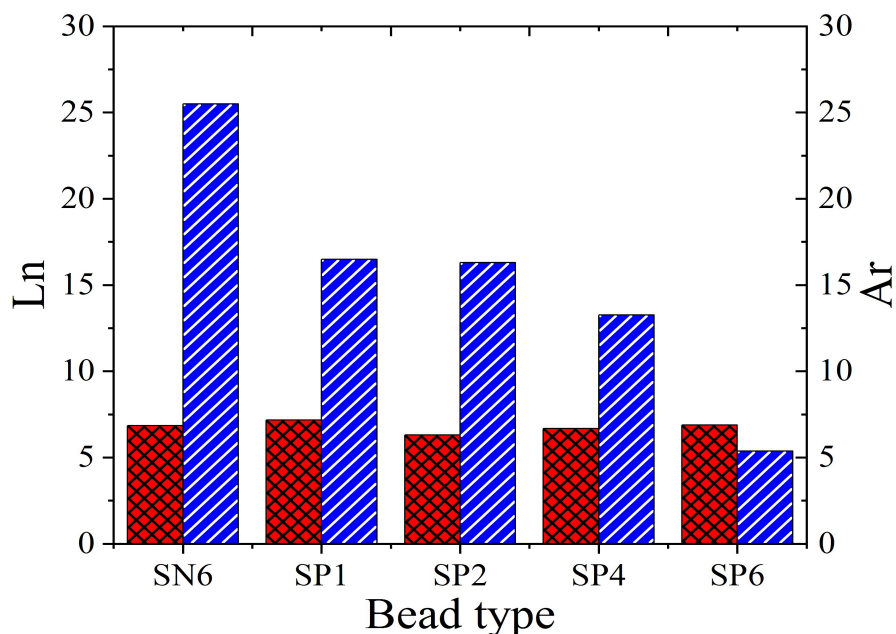


Figure S8: Relative error in CG density profiles of TPS constituents for TPS–TMA–MMT composite The Ar and Ln were calculated using Equations 2 and 3, respectively. The integration was performed till the end of the first solvation shell (1 nm). left and right axes show relative percentage error in Ln and Ar , respectively.

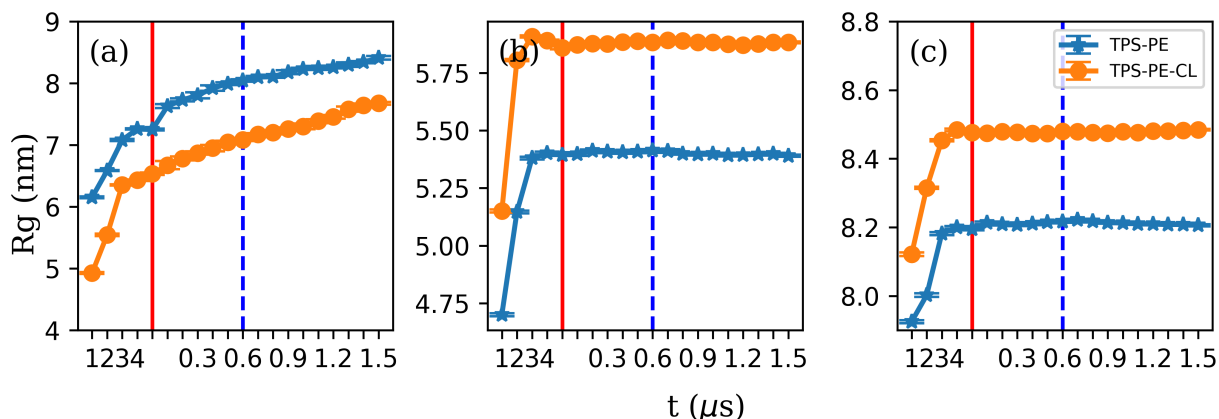


Figure S9: Dynamic changes in radius of gyration for polymers in TPS-PE melt and TPS-PE-CL composite system. (a), (b), and (c) show the time evolution of radius of gyration (R_g) of polyethylene (PE), amylose (AMY), and amylopectin (AMP), respectively. Data point were calculated in 100 ns blocks from CG MARTINI simulations of TPS-PE melt (\star) and TPS-PE-CL composite (\bullet) systems at 613 K and 1 bar. The x -axis indicates the equilibration cycle number, followed by a 25 ns NVT simulation (indicated by a horizontal ---), and the production run time scale in μs . The --- represents the end of the equilibration period, and data points following this line were used to calculate the average and error values reported in Table 5.

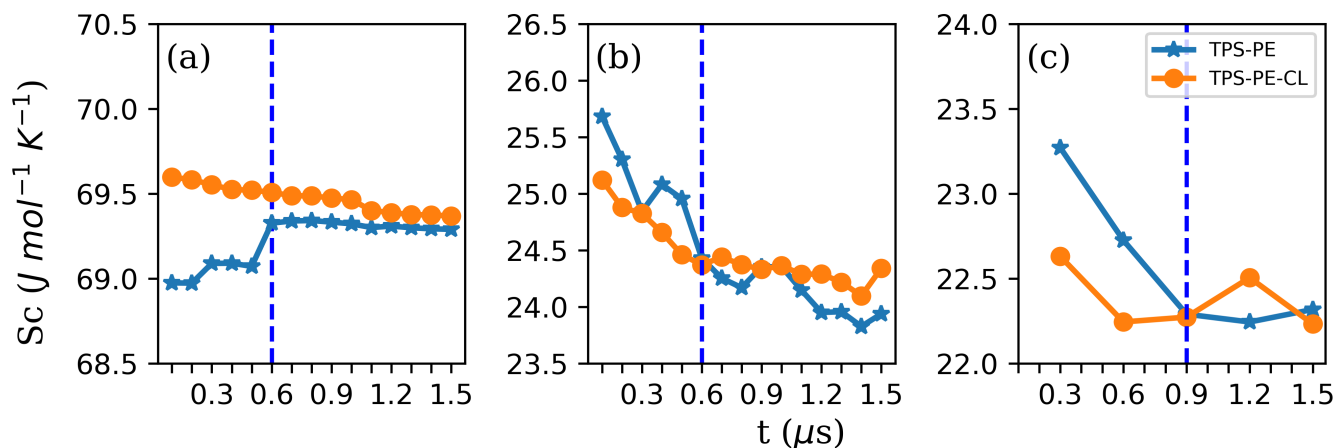


Figure S10: Temporal Profile polymer conformational entropy per CG bead in TPS-PE melt and TPS-PE-CL composite system. (a) The S_c of polyethylene, and (b) amylose was calculated in blocks of 100 ns. (c) A larger block size of 300 ns was used for amylopectin. All data are calculated using CG MARTINI simulation of TPS-PE (★) and TPS-PE-CL (●) systems at 613K and 1 bar. The --- represents the end of the equilibration period, and data points following this line were used to calculate the average and error values reported in Table 5.

Table S2: Two-body excess entropy of TPS melt system The two-body excess entropies for polymer-sorbitol pairs were calculated by integrating the RDFs (Figure S11) of the corresponding pairs in the TPS melt, using Equation 6.

System	TPS melt		
	Polymer-Polymer	Polymer-Sorbitol	Sorbitol-Sorbitol
AA	-1.33	-0.36	-0.52
CG	-1.30	-0.44	-0.98

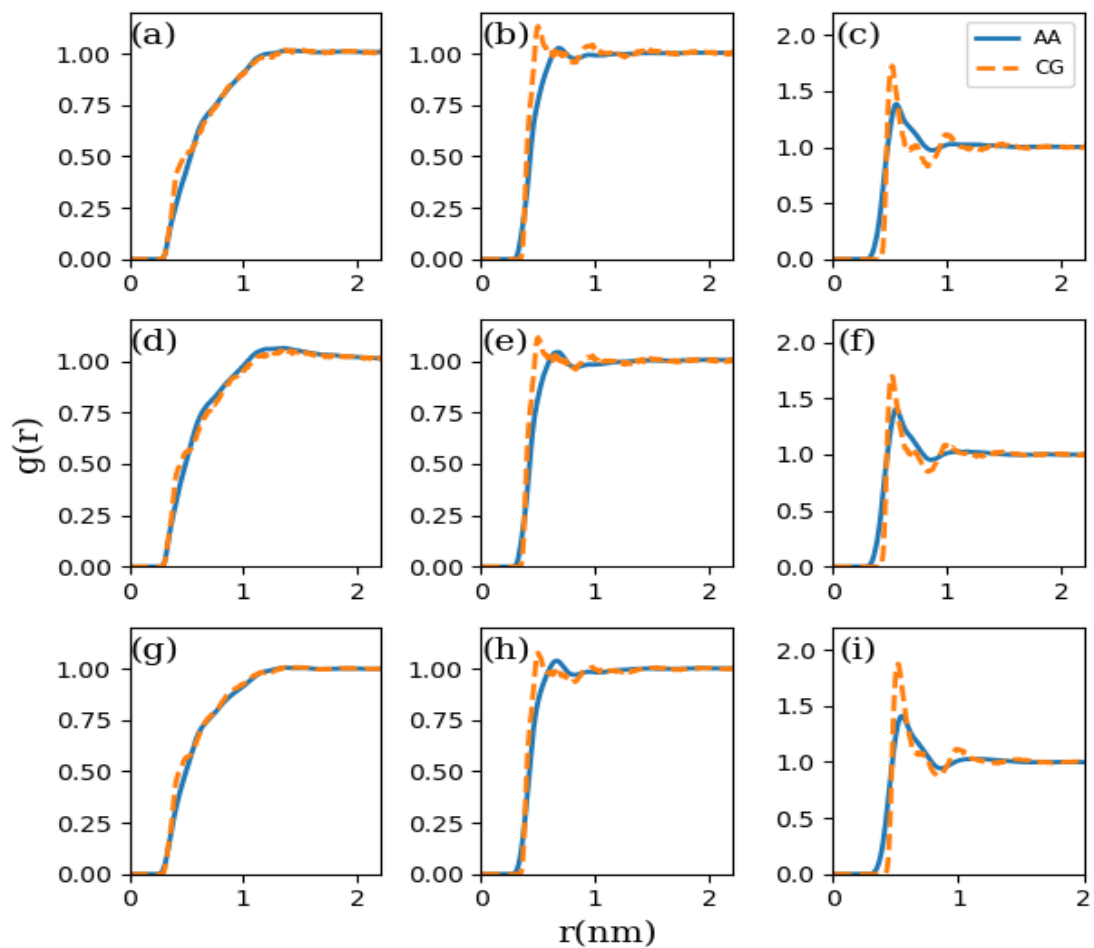


Figure S11: Radial distribution function for polymer-sorbitol pairs in TPS-TMA-MMT composite. (a), (d), and (g) show RDF for polymer-polymer pairs; (b), (e), and (h) show RDF for polymer-sorbitol pairs; and (c), f, and (i) show RDF for sorbitol-sorbitol pairs across the near-sheet, far-sheet, and melt. Data obtained from AA and CG of TPS melt and TPS-PY composite at 613 K and 1 bar.

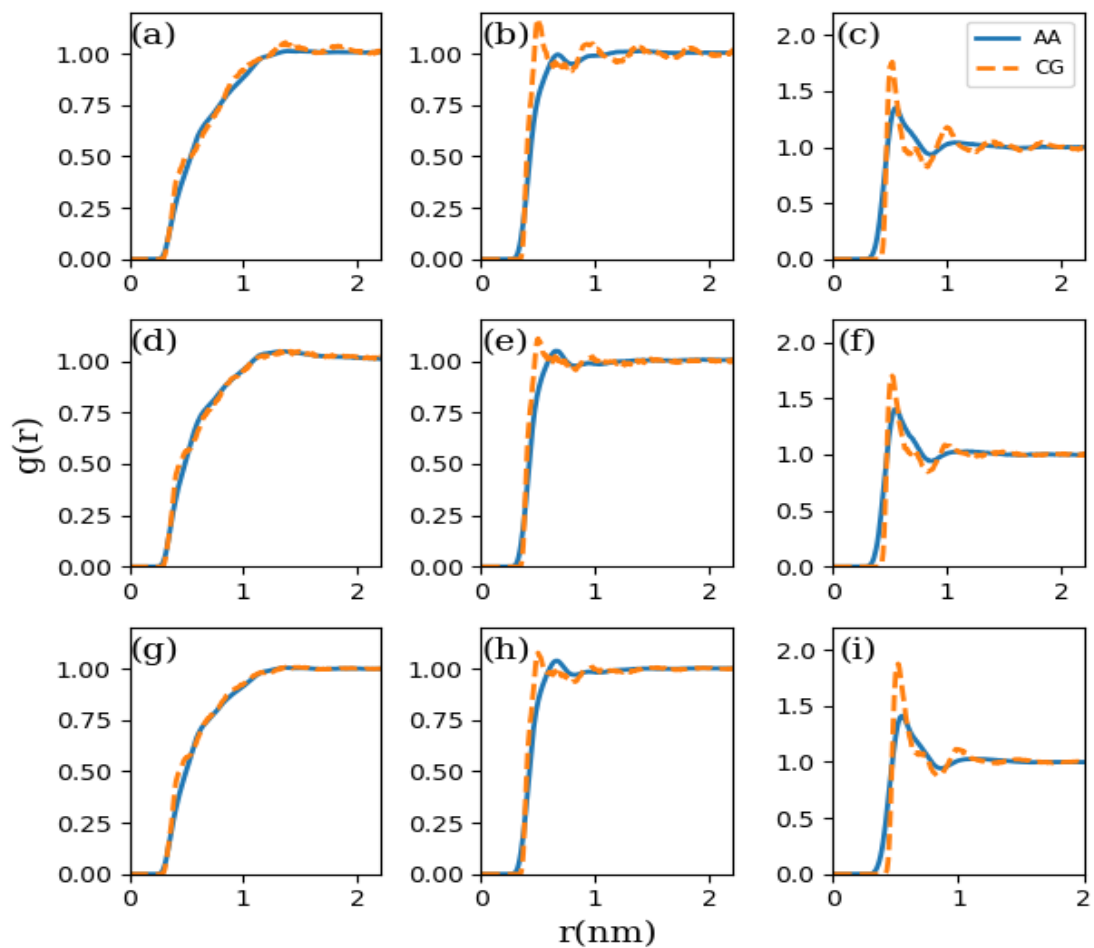


Figure S12: Radial distribution function for polymer-sorbitol pairs in TPS-TMA-MMT composite. (a), (d), and (g) show RDF for polymer-polymer pairs; (b), (e), and (h) show RDF for polymer-sorbitol pairs; and (c), (f), and (i) show RDF for sorbitol-sorbitol pairs across the near-sheet, far-sheet, and melt. Data obtained from AA and CG of TPS melt and TPS-TMA-MMT composite at 613 K and 1 bar.

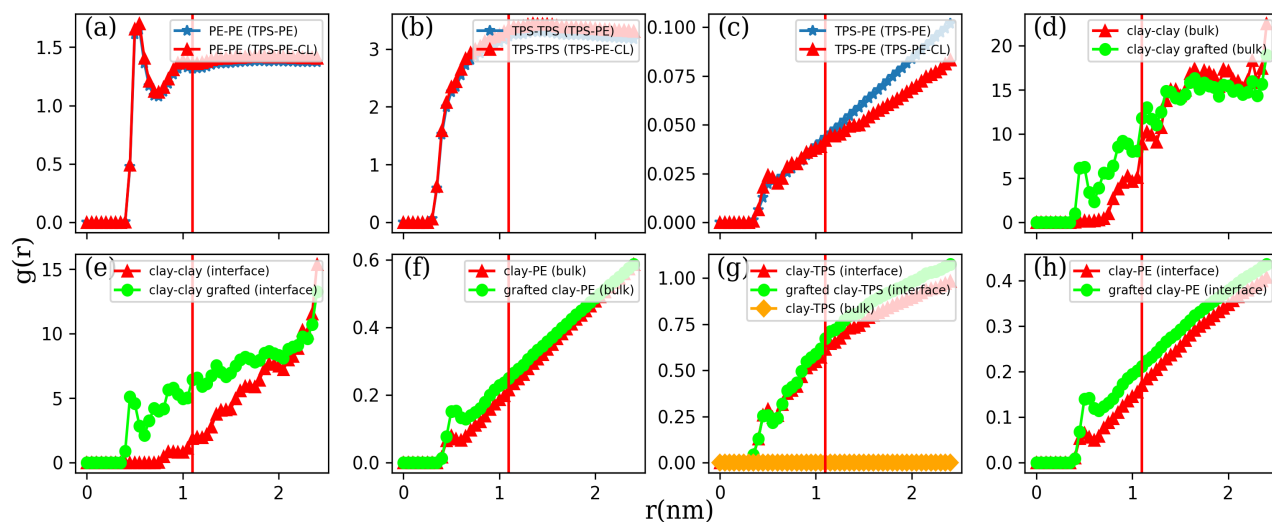


Figure S13: RDF of all possible pairs among TPS, PE, and clay in TPS-PE melt and TPS-PE-CL composite system. Radial distribution functions (RDFs) obtained from coarse-grained (CG) MARTINI simulations of TPS-PE melt (★) and TPS-PE-CL composite (▲, ●, and ◆) at 613 K and 1 bar. Panels present RDFs for: **(a)** PE-PE, **(b)** TPS-TPS, **(c)** TPS-PE, **(d)** clay-clay (in PE bulk phase), **(e)** interfacial clay-clay, **(f)** clay-PE (in PE bulk phase), **(g)** interfacial clay-TPS and bulk clay-interfacial TPS (◆), **(h)** clay-PE (at TPS-PE interface), and **(i)** interfacial clay-PE pairs.

TOC Graphic

Some journals require a graphical entry for the Table of Contents. This should be laid out “print ready” so that the text sizing is correct.

Inside the tocentry environment, the font used is Helvetica 8 pt, as required by *Journal of the American Chemical Society*.

The surrounding frame is 9 cm by 3.5 cm, which is the maximum permitted for *Journal of the American Chemical Society* graphical table of contents entries. The box will not resize if the content is too big; instead, it will overflow the edge of the box.

This box and the associated title will always be printed on a separate page at the end of the document.